Cell Stem Cell

Article

Mitochondrial dynamics maintain muscle stem cell regenerative competence throughout adult life by regulating metabolism and mitophagy

Graphical abstract

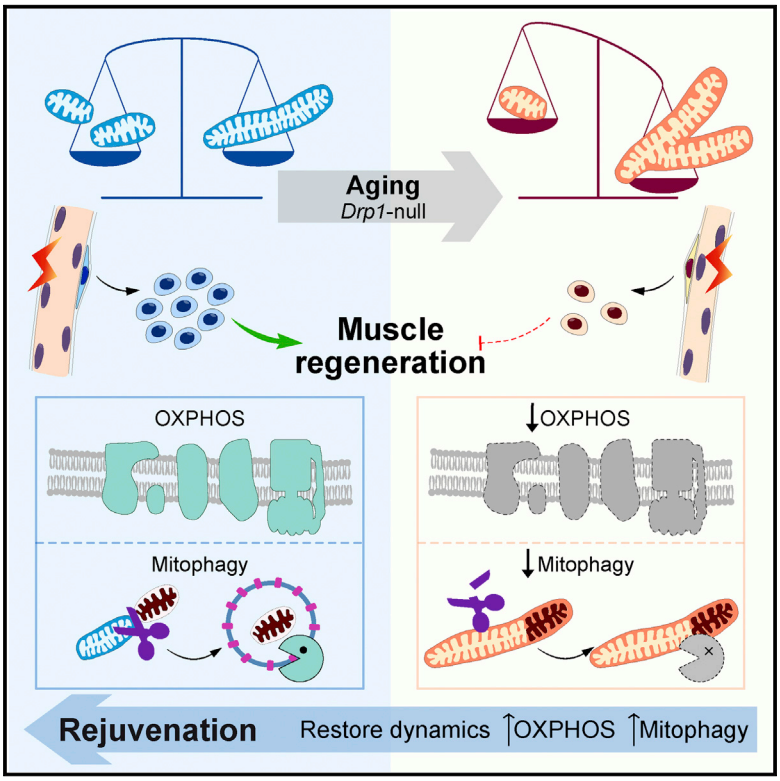

Authors

Xiaotong Hong, Joan Isern, Silvia Campanario, ..., Antonio L. Serrano, José A. Enríquez, Pura Muñoz-Cánoves

Correspondence

jaenriquez@cnic.es (J.A.E.), pura.munoz@cnic.es (P.M.-C.)

In brief

Hong et al. illustrate that mitochondrial dynamics are required for tissue regeneration. Mitochondrial fission facilitates stem cell function via OXPHOS and mitophagy regulation. The genetic (or aging-related) loss of the mitochondrial fission regulator DRP1 in muscle stem cells blunts their proliferation and regenerative capacity, whereas DRP1 re-establishment rescues these defects.

Highlights

- Mitochondrial fission increases in satellite cells (SCs) after muscle injury
- Mitochondrial fission boosts SC proliferation by inducing OXPHOS and proteostasis
- DRP1 loss in SCs (genetically or during aging) impairs muscle regeneration
- Normalizing mitochondrial dynamics in aged SCs restores muscle regeneration

Hong et al., 2022, Cell Stem Cell *29*, 1298–1314
September 1, 2022 © 2022 The Author(s). Published by Elsevier Inc.
https://doi.org/10.1016/j.stem.2022.07.009

CellPress

CellPress
OPEN ACCESS

Cell Stem Cell

Article

Mitochondrial dynamics maintain muscle stem cell regenerative competence throughout adult life by regulating metabolism and mitophagy

Xiaotong Hong,[1] Joan Isern,[1] Silvia Campanario,[1,2] Eusebio Perdiguero,[2] Ignacio Ramírez-Pardo,[1,2] Jessica Segalés,[2] Pablo Hernansanz-Agustín,[1] Andrea Curtabbi,[1] Oleg Deryagin,[2] Angela Pollán,[1] José A. González-Reyes,[3] José M. Villalba,[3] Marco Sandri,[4,5] Antonio L. Serrano,[2] José A. Enríquez,[1,6,*] and Pura Muñoz-Cánoves[1,2,7,8,9,*]

[1]Centro Nacional de Investigaciones Cardiovasculares (CNIC), 28029 Madrid, Spain
[2]Department of Experimental and Health Sciences, Pompeu Fabra University (UPF), CIBERNED, 08003 Barcelona, Spain
[3]Departamento de Biología Celular, Fisiología e Inmunología, Universidad de Córdoba, 14014 Córdoba, Spain
[4]Venetian Institute of Molecular Medicine, 35129 Padova, Italy
[5]Department of Biomedical Sciences, University of Padova, 35100 Padova, Italy
[6]CIBERFES, Madrid, Spain
[7]ICREA, 08003 Barcelona, Spain
[8]Altos Labs, San Diego, CA, USA
[9]Lead contact
*Correspondence: jaenriquez@cnic.es (J.A.E.), pura.munoz@cnic.es (P.M.-C.)
https://doi.org/10.1016/j.stem.2022.07.009

SUMMARY

Skeletal muscle regeneration depends on the correct expansion of resident quiescent stem cells (satellite cells), a process that becomes less efficient with aging. Here, we show that mitochondrial dynamics are essential for the successful regenerative capacity of satellite cells. The loss of mitochondrial fission in satellite cells—due to aging or genetic impairment—deregulates the mitochondrial electron transport chain (ETC), leading to inefficient oxidative phosphorylation (OXPHOS) metabolism and mitophagy and increased oxidative stress. This state results in muscle regenerative failure, which is caused by the reduced proliferation and functional loss of satellite cells. Regenerative functions can be restored in fission-impaired or aged satellite cells by the re-establishment of mitochondrial dynamics (by activating fission or preventing fusion), OXPHOS, or mitophagy. Thus, mitochondrial shape and physical networking controls stem cell regenerative functions by regulating metabolism and proteostasis. As mitochondrial fission occurs less frequently in the satellite cells in older humans, our findings have implications for regeneration therapies in sarcopenia.

INTRODUCTION

Skeletal muscle satellite cells (SCs) maintain and regenerate muscle tissue and are normally kept in a state of quiescence (e.g., a reversible G_0-like arrested state) throughout life. Upon injury, quiescent SCs (QSCs) rapidly activate and proliferate, thereby generating sufficient progeny to form new fibers and reconstruct the damaged tissue (reviewed in the studies conducted by Evano and Tajbakhsh, 2018; Galliot et al., 2017; and Sousa-Victor et al., 2020). This quiescence-to-proliferation transition becomes defective with aging, in yet unknown ways.

Proteostatic and metabolic regulation of muscle SCs is essential for maintaining their quiescence in homeostasis as well as for their capacity to activate and proliferate to regenerate damaged tissue (Chandel et al., 2016; García-Prat et al., 2017). Autophagy is a major proteostatic activity needed to maintain SCs in quiescence (García-Prat et al., 2016), which is further induced after injury to meet stem cell proliferative and metabolic demands (Tang and Rando, 2014; White et al., 2018). In fact, genetic ablation of autophagy perturbs mitochondrial function and ATP production (García-Prat et al., 2016; Tang and Rando, 2014). Previous studies have provided evidence of a SC metabolic switch upon exit from quiescence (Pala et al., 2018; Ryall et al., 2015). With aging, autophagy activity declines, leading to the accumulation of damaged cellular components (including mitochondria) (García-Prat et al., 2017) and correlating with changes in metabolism (Pala et al., 2018; Sahu et al., 2018; Zhang et al., 2016), which may underlie the impaired capacity to regenerate damaged muscle (reviewed in the studies conducted by Hong et al., 2022 and Sousa-Victor et al., 2022).

Mitochondria have a major role in producing adenosine triphosphate (ATP) through oxidative phosphorylation (OXPHOS) via the mitochondrial electron transport chain (ETC). They are also central hubs of carbohydrate, lipid, and amino-acid metabolism and are involved in essential cellular functions, such as reactive-oxygen-species (ROS) production and signaling (Hamanaka and Chandel, 2010; Shadel and Horvath, 2015), calcium homeostasis (Duchen, 2000; Giorgi et al., 2018; Rizzuto et al., 2012), and programed

 © 2022 The Author(s). Published by Elsevier Inc.
This is an open access article under the CC BY-NC-ND license (http://creativecommons.org/licenses/by-nc-nd/4.0/).

CellPress
OPEN ACCESS

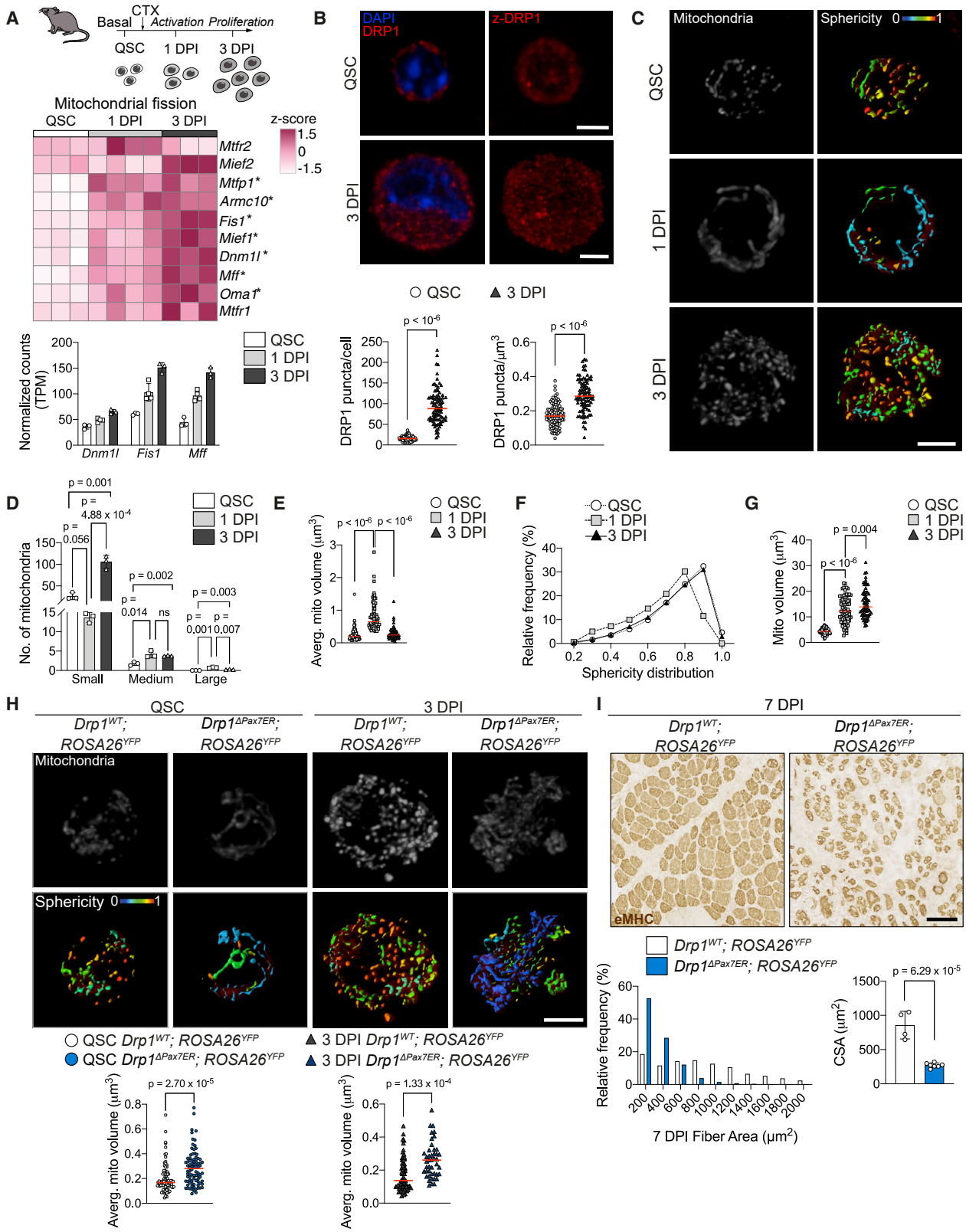

(legend on next page)

cell death (Hockenbery et al., 1990; Liu et al., 1996). To fulfill these functions, mitochondria actively remodel their morphology via dynamic fusion and fission (generally referred to as mitochondrial dynamics) (Detmer and Chan, 2007; Giacomello et al., 2020; Rambold and Pearce, 2018) in coordination with their metabolism and quality-control mechanisms (Adebayo et al., 2021; Djalalvandi and Scorrano, 2022; Rambold and Pearce, 2018). Fusion is driven by the outer membrane GTPases, by mitofusin (MFN) 1 and 2, and by the inner membrane protein optic atrophy 1 (OPA1). In turn, fission requires dynamin-related protein (DRP1), which is a cytosolic GTPase that is recruited to the outer mitochondria at ER-marked sites and facilitates mitochondrial constriction via the formation of GTP-dependent mitochondrial fission site by oligomerization (Chan, 2012; Youle and van der Bliek, 2012). An efficiently working mitochondrial fission machinery allows for the proper segregation of dysfunctional components of the mitochondrial network and facilitates their degradation via autophagy (i.e., mitophagy) (Toyama et al., 2016; Twig et al., 2008; Zhang and Lin, 2016). However, we still do not understand if this is causally linked to stem cell functions and/or their age-associated decline.

Using a genetic model ablating *Drp1* in SCs, we show that mitochondrial dynamics, and in particular mitochondrial fission, are required for efficient expansion of SCs during muscle regeneration, by dictating mitochondrial metabolism and proteostatic fitness. We further reveal that reduced mitochondrial fission underlies reduced SC regeneration with aging and that it can be rescued by stimulating mitochondrial OXPHOS and mitophagy.

RESULTS

Satellite cell mitochondrial fission is required for muscle regeneration

To study how SCs respond to muscle injury at the transcriptional level, we performed an RNA sequencing (RNA-seq)-coupled bioinformatic analysis of SCs isolated by fluorescence-activated cell sorting (FACS). SCs were taken from young mice from unperturbed muscle (QSCs) or from regenerating muscle at 1 or 3 days postinjury (DPI) (1DPI-SCs or 3DPI-SCs), which are in an activated or proliferating state, respectively (Figures 1A and S1A). As expected, pathways related to cell cycle and proliferation were enriched in 1DPI-SCs and 3DPI-SCs as compared with QSCs, with a simultaneous boost of various energy-producing pathways (glycolysis, tricarboxylic acid [TCA] cycle, and OXPHOS) (Figure S1B), while fatty-acid metabolism switched from very-long-chain fatty-acid utilization and fatty-acid synthesis to mitochondrial β-oxidation (Figure S1B) (see also Pala et al., 2018; Ryall et al., 2015). We found a previously unnoticed signature of upregulated genes related to mitochondrial fission in 1DPI-SCs, which was further augmented in 3DPI-SCs; among these, the expression levels of mitochondrial fission regulator (*Drp1*/*Dnml1*) and its receptors mitochondrial fission 1 (*Fis1*) and mitochondrial fission factor (*Mff*) were significantly enhanced during the quiescence-to-proliferation transition (Figure 1A). Consistent with the RNA-seq results, the DRP1 protein level was significantly upregulated in 3DPI-SCs as compared with QSCs (Figure 1B), and this increase in DRP1 expression exceeded the increase in cell growth (Figure 1B), suggesting a predominant involvement of mitochondrial fission during this transition.

To examine mitochondria remodeling in SCs during this injury-induced transition, FACS-isolated SCs were stained with MitoTracker Red CMXRos (García-Prat et al., 2016), and labeled mitochondria were imaged and then analyzed by 3D volume reconstruction (Figure 1C and Video S1). QSCs had a low amount of mitochondria, which were either small-sized (~95% had a volume < 0.5 μm^3) or medium-sized (~5% had a volume from 0.5 to 4 μm^3); almost no mitochondria were large-sized (< 0.1% had a volume of >4 μm^3) (Figures 1D and S1C). In contrast, 1DPI-SCs had more medium and large mitochondria, with a larger average size (Figures 1D and 1E) and a more complex network with reduced sphericity (Figure 1F), indicative of fusion during the early activation stage. In proliferating 3DPI-SCs, the total volume of mitochondria increased significantly, suggesting induction of mitochondrial biogenesis (Figure 1G). Strikingly, 3DPI-SCs contained a higher number of small, more spherical mitochondria (and very few large mitochondria) than 1DPI-SCs (Figures 1D and S1C), indicating that the proliferating SCs at 3 DPI had low mitochondrial complexity. These results suggested that mitochondria actively reorganize their shape when SCs exit quiescence after injury and become smaller and less complex during the key proliferative stage.

To investigate if the disruption of mitochondrial fission machinery could causally alter SC functions, we crossed a floxed mouse line for *Drp1* with a tamoxifen (TMX)-inducible satellite-cell-specific *Pax7^{ER}-Rosa26-YFP* reporter mouse line, giving *Drp1$^{\Delta Pax7ER}$;ROSA26^{YFP}* (hereafter, *Drp1$^{\Delta Pax7ER}$*). Freshly sorted YFP$^+$ SCs

Figure 1. Satellite cell mitochondrial fission is required for muscle regeneration

(A) Schematics of the isolation of quiescent (QSCs), activated (1DPI-SCs), and proliferating (3DPI-SCs) satellite cells from the muscles of young mice (top). Muscle injury was induced by cardiotoxin (CTX). Heatmap representing the expression of mitochondrial fission genes (middle). Gene expression levels are transcripts per million (TPM) (bottom). * represents differentially expressed (DE) genes (adjusted p value < 0.05).

(B) Representative images (top) and quantification (bottom) of DRP1 protein puncta in QSCs and 3DPI-SCs by immunofluorescence (IF).

(C) Representative images of MitoTracker IF (left) and 3D-reconstructed mitochondrial network (right) in QSCs, 1DPI-SCs, and 3DPI-SCs. Reconstructed mitochondria are colored by their sphericity (0–1).

(D) Average number of mitochondria in each cell, categorized as small (< 0.5 μm^3), medium (0.5–4 μm^3), or large (> 4 μm^3).

(E–G) Mitochondrial analyses of QSCs, 1DPI-SCs, or 3DPI-SCs, showing the quantification of average mitochondrial volume in each cell (E), distribution curves of mitochondrial sphericity (F), and reconstructed total mitochondrial volume per cell (G).

(H) Representative images of MitoTracker IF (top) and 3D-reconstructed mitochondrial network (bottom) in *Drp1^{WT}* or *Drp1$^{\Delta Pax7ER}$* QSCs and 3DPI-SCs. Reconstructed mitochondria are colored by their sphericity (0–1).

(I) Representative images of embryonic myosin heavy-chain (eMHC) staining by immunohistochemistry (IHC) in 7-DPI muscle from *Drp1^{WT}* and *Drp1$^{\Delta Pax7ER}$* mice (top), and the quantification of eMHC$^+$ fiber size represented in size distribution (lower left) and average cross-section area (CSA) (lower right).

Data represent n = 3–7 mice and show mean ± SD. p values were determined by two-tailed unpaired t test. Scale bars: 3 μm in (B), (C), and (H) and 50 μm in (I). See also Figures 2 and S1 and Video S1.

CellPress
OPEN ACCESS

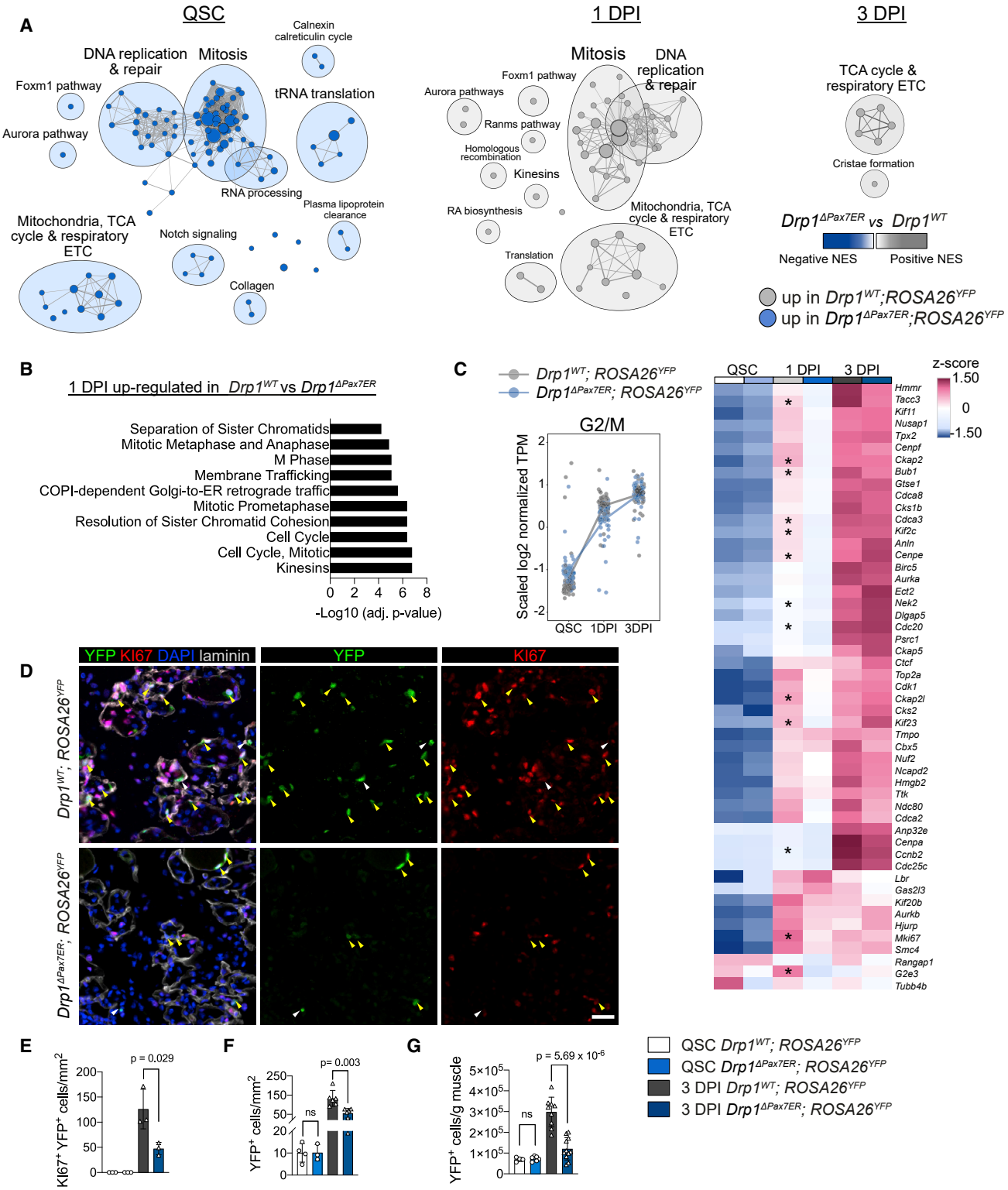

Figure 2. Mitochondrial fission allows quiescence exit and satellite cell expansion

(A) Enrichment map of gene sets enriched in *Drp1*$^{\Delta Pax7ER}$ satellite cells (blue) or *Drp1*^{WT} satellite cells (gray) obtained from resting muscle (QSCs) or injured (1 DPI or 3 DPI) limb muscles. Gray node, positive NES; blue node, negative NES. Node size is proportional to the number of genes identified in each gene set (minimum 10 genes/gene set). Clusters were automatically annotated using the Autoannotate app in Cytoscape.

(B) Pathway analysis of DE genes upregulated in *Drp1*^{WT} versus *Drp1*$^{\Delta Pax7ER}$ 1DPI-SCs. Pathway analysis was carried out in g:Profiler; top Reactome pathways are presented.

(legend continued on next page)

from muscle of TMX-treated *Drp1*$^{\Delta Pax7ER}$ mice showed efficient deletion of *Drp1* (Figures S1D–S1F). 3D analysis of the mitochondrial shape in YFP$^+$-sorted QSCs or 3DPI-SCs revealed that the fission-impaired *Drp1*$^{\Delta Pax7ER}$ QSCs showed increased average mitochondrial volume and decreased sphericity but no major changes in mitochondrial size by category, as compared with those of wild-type (WT) (*Drp1*^{WT}*; ROSA26*^{YFP}*;* hereafter, *Drp1*^{WT}) mice (Figures 1H and S1G). In contrast, 3DPI-SCs from *Drp1*$^{\Delta Pax7ER}$ mice had more medium- to large-sized mitochondria, and fewer small mitochondria, than 3DPI-SCs from *Drp1*^{WT} mice (Figure S1H), coinciding with the increase in average mitochondrial volume during the stem cell expansion phase (Figure 1H). Overall, the mitochondrial shape was more complex in SCs from *Drp1*$^{\Delta Pax7ER}$ mice than from *Drp1*^{WT} mice, with lower mitochondrial sphericity (Figure S1H), thus confirming that increased mitochondrial fusion occurred in the absence of *Drp1*. Transmission electron microscopy (TEM) analysis of proliferating YFP$^+$ *Drp1*$^{\Delta Pax7ER}$ cultured SCs showed elongated mitochondria with abnormal organization of the mitochondrial ultrastructure, showing concentric ("onion-shaped") mitochondria cristae (Figure S1I), with disorganized cristae in (but not all) mitochondria (Figure S1I). Similar shapes have been reported in cells with mutations in the mitochondrial contact site and cristae organizing system (MICOS) (John et al., 2005; Li et al., 2016; Vincent et al., 2016) and in cells with genetically induced elongated mitochondria (Fissi et al., 2018; Liaghati et al., 2021), suggesting that proteins regulating mitochondrial dynamics participate in mitochondrial ultrastructure maintenance. Finally, immunofluorescence (IF) imaging of proliferating *Drp1*$^{\Delta Pax7ER}$ SCs from regenerating muscle clearly showed a hyperfused mitochondria network (Figure 1J).

The number of QSCs was similar in *Drp1*$^{\Delta Pax7ER}$ and WT mice (Figure S2A). However, at 5 DPI and 7 DPI, *Drp1*$^{\Delta Pax7ER}$ muscle had smaller myofibers expressing embryonic myosin heavy chain (eMHC) (indicative of newly formed, regenerating myofibers) as compared with WT; this persisted up to 14 DPI (Figures 1I, S2B, and S2C). These results indicate that SC mitochondria change their shape as the cells progress from quiescence to proliferation and that mitochondrial fission is indispensable for efficient muscle regeneration.

Mitochondrial fission permits satellite cell expansion after tissue injury

To understand how loss of mitochondrial fission impairs satellite-cell-dependent muscle repair, we performed RNA-seq of YFP$^+$-sorted QSCs, 1DPI-SCs, and 3DPI-SCs from muscles of young *Drp1*$^{\Delta Pax7ER}$ or *Drp1*^{WT} mice. Based on transcriptome analysis of differentially expressed (DE) genes, we built a DRP1-centered interaction network of pathways related to cell cycle, metabolism, stress response, and proteostasis (Figures S3A–S3C). Gene set enrichment analysis (GSEA) and Cytoscape EnrichmentMap analysis confirmed alterations in these main pathways in each SC state in the absence of *Drp1* (Figure 2A). Compared to *Drp1*^{WT} QSCs, *Drp1*$^{\Delta Pax7ER}$ QSCs were enriched in genes related to cell division (including mitosis, DNA replication and repair, the Foxm1 and Aurora pathways, and RNA processing) and metabolism (including TCA cycle and the ETC). Indeed, the transcriptome of *Drp1*$^{\Delta Pax7ER}$ QSCs, but not of *Drp1*^{WT} QSCs, was closer to the reported gene signature of primed QSCs than to the more dormant/genuine QSCs (García-Prat et al., 2020; Rocheteau et al., 2012) (Figure S3D). Furthermore, the pathways upregulated in *Drp1*$^{\Delta Pax7ER}$ QSCs (versus *Drp1*^{WT} QSCs) were only upregulated in *Drp1*^{WT} cells after injury (Figures 2A and S3E). Nevertheless, in resting muscle, *Drp1*$^{\Delta Pax7ER}$ QSCs: (1) were not "alerted" (Rodgers et al., 2014) or proliferating (shown by negative immunostaining for phosphorylated S6 or KI67, respectively) (Figures S3F and S3G); (2) had no DNA damage (shown by γ-H2AX staining) (Figure S3H); and (3) did not have increased RNA content (shown by pyronin Y staining) (Figure S3I). Thus, in resting muscle, SCs with disrupted mitochondrial fission are "molecularly/transcriptionally primed" for activation but do not functionally leave the quiescence state.

Of note, 1DPI-SCs from *Drp1*$^{\Delta Pax7ER}$ mice expressed lower levels of genes related to cell cycle and cell proliferation than those from *Drp1*^{WT} mice (Figures 2A, 2B, and S3C). Additionally, although expression of G2/M-related genes was high in *Drp1*$^{\Delta Pax7ER}$ QSCs (Figure 2C), it showed a blunted slope in *Drp1*$^{\Delta Pax7ER}$ 1DPI-SCs but increased dramatically in *Drp1*^{WT} 1DPI-SCs; these differences were attenuated at 3 DPI (Figure 2C).

Both *Drp1*^{WT} and *Drp1*$^{\Delta Pax7ER}$ 1DPI-SCs expressed comparable levels of SC activation markers (which are absent in QSCs) (Figure S3J), with a similar number of SCs expressing MYOD protein (a marker of activation) (Figure S3K), further supporting the hypothesis that *Drp1*$^{\Delta Pax7ER}$ SCs have no defects in activating from quiescence. In contrast, at the myogenic stage, *Drp1*$^{\Delta Pax7ER}$ muscle had a reduced number of proliferating (KI67$^+$) YFP$^+$ 3DPI-SCs as compared with *Drp1*^{WT} muscle, as shown by both immunostaining and YFP$^+$ FACS-sorting (Figures 2D–2G). No increased levels of cell death were observed (Figure S3L). Thus, the muscle regenerative defect in *Drp1*$^{\Delta Pax7ER}$ mice after injury cannot be attributed to a defect in early activation but is rather caused by the subsequent incapacity of SCs to proliferate adequately and generate sufficient progeny to form new fibers when mitochondrial fission is blunted.

Mitochondrial fission allows satellite cells to induce OXPHOS metabolism during muscle regeneration

Comparison of our RNA-seq data with an inventory of 1,140 mitochondrial genes (MitoCarta3.0) showed a high upregulation of mitochondrial genes in *Drp1*^{WT} 1DPI-SCs and *Drp1*^{WT} 3DPI-SCs as compared with *Drp1*^{WT} QSCs (Figure S4A), while

(C) *Z* score analysis of G2/M cell-cycle genes during analyzed states in *Drp1*^{WT} and *Drp1*$^{\Delta Pax7ER}$ satellite cells, presented as dot graph (left) or heatmap (right). Each dot represents *Z* score trajectory of a single gene, and the thick lines indicate the average *Z* score trajectory of the pathway. *DE genes (adjusted p value < 0.05).

(D) Representative images of YFP, KI67, 4′,6-diamidino-2-phenylindole (DAPI), and laminin IF staining of *Drp1*^{WT} and *Drp1*$^{\Delta Pax7ER}$ 3-DPI TA muscles. Scale bars, 50 μm.

(E–G) Quantification of proliferating YFP$^+$ satellite cells (KI67$^+$YFP$^+$) (E), total satellite cells (F) from (D), and YFP$^+$ satellite cells obtained by FACS (G) from muscles of *Drp1*$^{\Delta Pax7ER}$ or *Drp1*^{WT} mice in quiescence (QSCs) and at 3 DPI.

Data represent n = 3–11 mice and show mean ± SD. p values were determined by a two-tailed unpaired t test. See also Figure S3 and Tables S1 and S2.

analyses of DE genes identified upregulation of mitochondrial biogenesis and metabolism pathways (Figure S4B). Of interest, almost all genes encoding the ETC complex subunits were upregulated in 1DPI-SCs (i.e., after exiting quiescence), with a peak in 3DPI-SCs (Figure S4C), supporting the hypothesis that SCs adapt their metabolism toward OXPHOS for proliferation. In contrast, *Drp1*$^{\Delta Pax7ER}$ QSCs showed increased expression of the TCA cycle, ETC, cristae formation, and mitosis-related genes as compared with *Drp1*^{WT} QSCs (Figure 2A), which is in agreement with their molecularly primed state (Figure S3D). In response to injury, however, GSEA and Cytoscape analyses showed that these pathways in *Drp1*$^{\Delta Pax7ER}$ 1DPI-SCs were not as highly induced as in *Drp1*^{WT} 1DP1-SCs (Figure 2A). Further, at 3 DPI, the TCA and ETC pathway genes remained downregulated in *Drp1*$^{\Delta Pax7ER}$ as compared with *Drp1*^{WT} SCs (Figure 2A). In particular, genes encoding the mitochondrial TCA pathway and ETC complex IV proteins (e.g., *Pfkm*, *Cox7a1*, *Cox7a2*, and *Cox10*) were downregulated in *Drp1*$^{\Delta Pax7ER}$ 3DPI-SCs, whereas *Pck2* (which is involved in gluconeogenesis) was upregulated (Table S1). Consistent with this, all five ETC complexes and OXPHOS genes were upregulated in *Drp1*$^{\Delta Pax7ER}$ as compared with *Drp1*^{WT} QSCs, and this trend changed at 1 DPI and 3 DPI (Figures 3A and 3B).

Functional cellular respiratory analysis by Seahorse revealed that while *Drp1*$^{\Delta Pax7ER}$ QSCs had basal and maximal oxygen-consumption rates (OCRs) similar to *Drp1*^{WT} QSCs, they tended to have a higher proton leak (less ATP production by OXPHOS) (Figures 3C and S4D), in accordance to the fact that *Drp1*$^{\Delta Pax7ER}$ QSCs are primed but not functionally activated. However, in *Drp1*$^{\Delta Pax7ER}$ 3DPI-SCs (as compared with *Drp1*^{WT} 3DPI-SCs), we observed a dramatic reduction of cellular maximal respiration and spare respiratory capacity (Figures 3D and S4D), consistent with the RNA-seq data showing significantly lower expression of OXPHOS genes. Nonmitochondrial respiration was also lower in *Drp1*$^{\Delta Pax7E}$ than *Drp1*^{WT} SCs, but no significant differences were detected in basal OCR and complex V activity (ATP-associated OCR) between the genotypes (Figure S4D). Oxygen-consumption analysis of cultured YFP^{+} SCs revealed a global impairment of the mitochondrial respiration in *Drp1*$^{\Delta Pax7ER}$ SCs, marked by significantly reduced mitochondrial ETC complex I, II, and IV activities (Figure 3E). On the other hand, the total cellular ATP levels were similar in SCs of both genotypes (Figure S4E), indicating that *Drp1*$^{\Delta Pax7ER}$ SCs use other energy sources for ATP production.

Although unstudied in stem cells, the synthesis and assembly of the ETC are known to depend on the proportion and distribution of the mtDNA, along with the mitochondrial network (Ishihara et al., 2015; Parone et al., 2008). We found that *Drp1*$^{\Delta Pax7ER}$ QSCs had a lower mtDNA copy number than *Drp1*^{WT} QSCs (Figure 3F), despite similar mitochondrial volumes (Figure S4F). Further, at 3 DPI, the mtDNA content increased in both genotypes, but the copy number remained lower in *Drp1*$^{\Delta Pax7ER}$ than in *Drp1*^{WT} cells (Figure 3F), indicating inefficient mtDNA replication in proliferating SCs when mitochondrial fission was impaired. More surprisingly, both the size and the distribution of mitochondrial nucleoids (i.e., the mtDNA protein packaging complexes; Farge et al., 2014) were aberrant in *Drp1*$^{\Delta Pax7ER}$ QSCs, with fewer and larger nucleoids (Figures 3G, S4G, and S4H). This nucleoid imbalance was further exacerbated in 3DPI-SCs, as shown by the abnormally enlarged nucleoids (Figure 3G). Thus, following injury, mitochondrial fission blockade in SCs impedes normal mitochondrial metabolic reprogramming and induces the presence of abnormal nucleoids, which together could underpin the low efficiency of the ETC and OXPHOS during the regenerative demand following injury.

Mitochondrial fission permits mitophagy in satellite cells during muscle regeneration

Our transcriptomic analysis also identified numerous stress-response- and proteostasis-related genes, such as the increased expression of asparagine synthetase (*Asns*), which could reflect a need to dispose of the aspartate accumulated due to mitochondrial dysfunction and a reduced TCA cycle flux (Corrado et al., 2021) (Table S1; Figure S3C). Accordingly, we observed significantly increased cellular and mitochondrial ROS levels in the *Drp1*$^{\Delta Pax7ER}$ SCs, with evident accumulations of ROS puncta in the mitochondrial matrix (Figure 4A), suggesting increased levels of malfunctioning or damaged mitochondria upon *Drp1* loss. To analyze these possibilities, we treated freshly sorted SCs from *Drp1*$^{\Delta Pax7ER}$ and *Drp1*^{WT} mice with the autophagy-flux inhibitor bafilomycin A, which blocks the elimination of autophagosomes by fusion with lysosomes (García-Prat et al., 2016). This treatment increased the LC3^{+} puncta (i.e., autophagosomes) in *Drp1*^{WT} but not *Drp1*$^{\Delta Pax7ER}$ SCs, indicating that autophagy is blunted in the absence of DRP1 (Figure 4B). Notably, mitophagy was also defective in *Drp1*$^{\Delta Pax7ER}$ SCs, as indicated by the accumulation of mitochondria inside autophagosomes (e.g., LC3-mitochondria co-localization in bafilomycin A-treated sorted cells) (Figure 4B). Consistent with this, p62 levels were increased in *Drp1*$^{\Delta Pax7ER}$ SCs, both on the cellular level and in mitochondria (Figure 4C), indicating increased accumulation of damaged mitochondria and other cellular components upon DRP1 loss that are not removed by the autophagy machinery. The signal for Parkin, a key regulator of the PINK1/Parkin-mediated mitophagy, was also significantly increased in *Drp1*$^{\Delta Pax7ER}$ SCs, but its co-localization in mitochondria was reduced as compared with *Drp1*^{WT} cells (Figure 4D). Of note, low mitochondrial membrane potential (MMP) can induce Parkin recruitment to the damaged mitochondria (Kuroda et al., 2012; Matsuda et al., 2010; Narendra et al., 2008; Okatsu et al., 2012); hence, the increased MMP in *Drp1*$^{\Delta Pax7ER}$ SCs (Figure S4I) may in part explain the cytoplasmic accumulation of Parkin in these cells. This loss of mitophagy when mitochondrial fission is impaired could also account for excessive ROS accumulation.

Transient adynamism restores the proliferative capacity of *Drp1*-null satellite cells

In cardiomyocytes, short-term forced mitochondrial adynamism can relieve the undesirable effects introduced by imbalanced mitochondrial dynamics (Song et al., 2017). To abrogate mitochondrial fusion, we genetically silenced *Mfn1* with a siRNA (si-*Mfn1*), which significantly reduced *Mfn1* expression (Figure S5A); this led to mitochondrial fragmentation in *Drp1*^{WT} SCs and a decreased average mitochondrial volume in *Drp1*$^{\Delta Pax7ER}$ cells (Figure 5A), suggesting that the enlarged mitochondrial network in *Drp1*-null SCs can be dissociated by repressing mitochondrial fusion. Importantly, in stem cell transplantation experiments in injured muscle, *Mfn1* silencing in YFP^{+} *Drp1*$^{\Delta Pax7ER}$ SCs increased the number

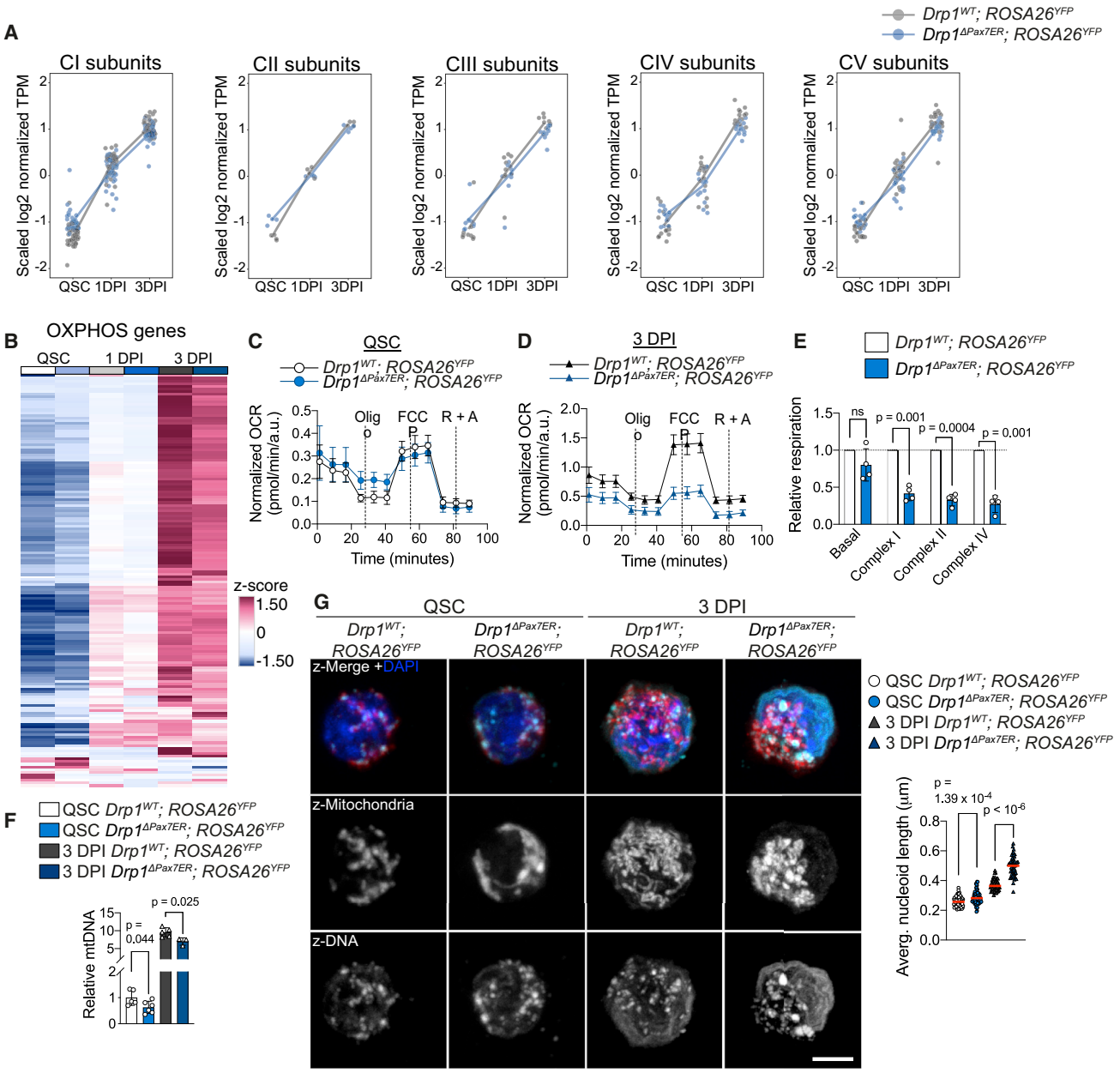

Figure 3. Impaired mitochondrial fission blunts OXPHOS metabolic reprogramming and mitophagy of satellite cells after muscle injury

(A) *Z* score analysis of electron transport chain (ETC) complex I–V subunit genes during the analyzed states in *Drp1*^{WT} and *Drp1*$^{\Delta Pax7ER}$ satellite cells, presented as dot graphs. Each dot represents the *Z* score of a single gene, and the thick lines show the average *Z* score trajectory of the pathway.

(B) *Z* score analysis of total OXPHOS genes in the analyzed states in *Drp1*^{WT} and *Drp1*$^{\Delta Pax7ER}$ satellite cells presented as a heatmap.

(C and D) Normalized oxygen-consumption rates (OCRs) of QSCs (C) and 3DPI-SCs (D) from *Drp1*^{WT} compared with *Drp1*$^{\Delta Pax7ER}$ mice at baseline and in response to oligomycin A (oligo), FCCP, or rotenone plus antimycin A (R + A). Data were obtained using Seahorse XF96 and normalized to protein level using CyQUANT cell-proliferation assay.

(E) Relative respiration of each mitochondrial ETC complex measured by Oxygraph (Oroboros). Values were normalized to cell numbers and to the levels of *Drp1*^{WT}.

(F) Copy numbers of mtDNA in QSCs or 3DPI-SCs from *Drp1*^{WT} or *Drp1*$^{\Delta Pax7ER}$ muscles (normalized to *Drp1*^{WT} QSC levels). mtDNA copy numbers were normalized to genomic DNA copy numbers, quantified by qPCR ($2^{-\Delta CT}$).

(G) Representative IF images (left) and quantification of average mitochondrial nucleoid length. Mitochondria were detected with citrate synthase antibody. Scale bars: 3 µm.

Data represent n = 3–6 mice and show mean ± SD. p values were determined by a two-tailed unpaired t test. Gene lists in (A) and (B) are obtained from mouse MitoCarta3.0 database. See also Figure S4 and Table S2.

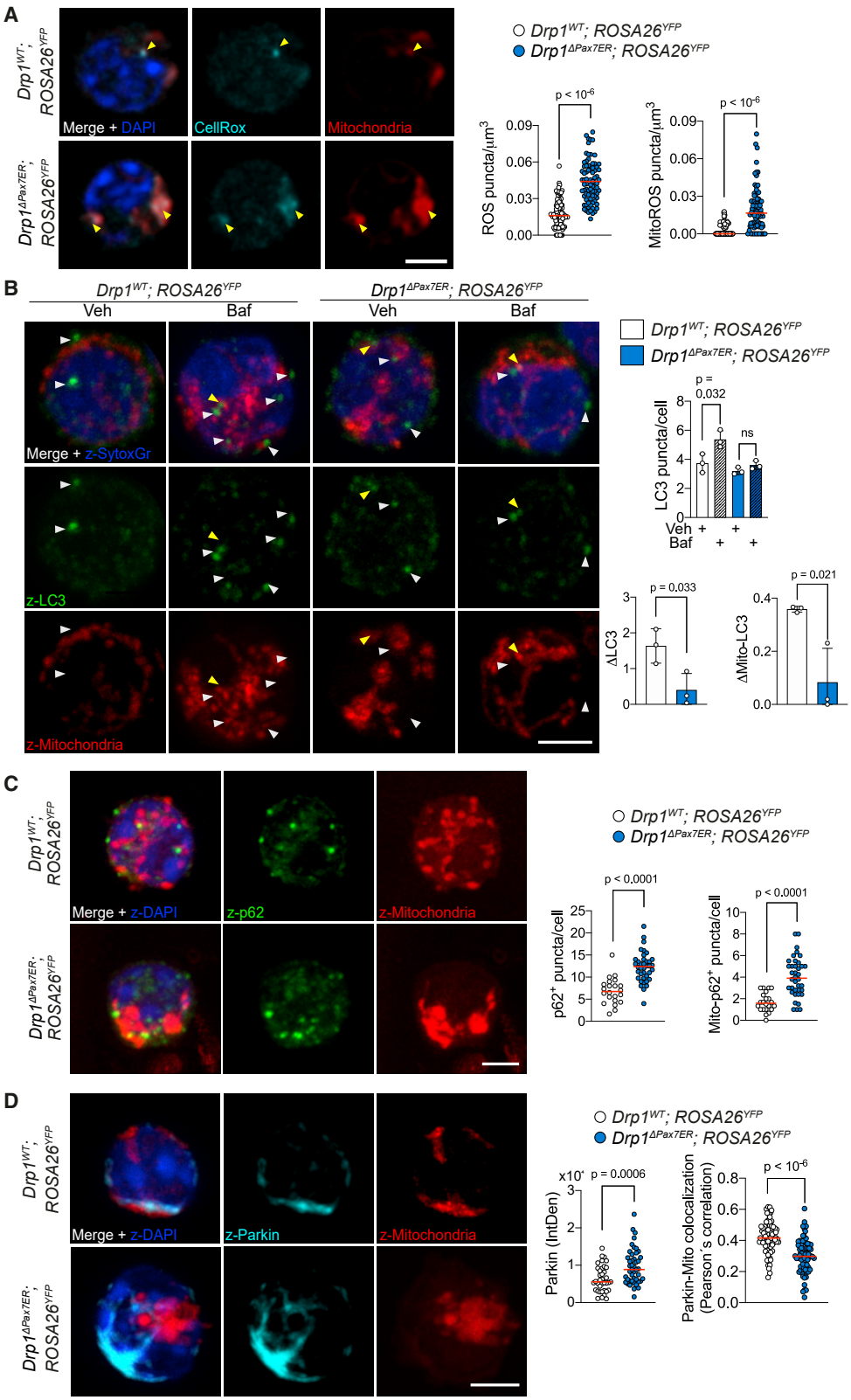

(legend on next page)

of YFP$^+$ cells in regenerating muscle after transplantation (Figure 5B) and increased the size of regenerating myofibers (Figure S5B). Conversely, only silencing *Mfn1* in WT SCs slightly reduced their engraftment capacity in regenerating muscle (Figure S5C). *Mfn1* silencing in *Drp1*$^{\Delta Pax7ER}$ SCs partially rescued the aggregation of mitochondrial nucleoids, giving a reduced average nucleoid length and reduced number of extremely large nucleoids (e.g., length > 0.8 μm) (Figure 5C), and increased the mitophagic flux and maximal respiration (Figures 5D and 5E). Thus, short-term forced mitochondrial adynamism improved the proliferative capacity of *Drp1*$^{\Delta Pax7ER}$ SCs, perhaps due to the joint effects of reduced mitochondrial nucleoid aggregation, improved mitochondrial respiratory capacity, and enhanced mitophagy.

Restoring OXPHOS and mitophagy rescues the regenerative failure of *Drp1*-null satellite cells

We next tested methods of improving OXPHOS and autophagy in *Drp1*$^{\Delta Pax7ER}$ SCs. Dichloroacetate (DCA) diverts glucose metabolism from lactic fermentation to the TCA cycle and mitochondrial OXPHOS. We confirmed that DCA treatment significantly increased OCR and mitochondrial ATP production rates in SCs (Figure S5D). Of note, daily DCA treatment (for 4 days) of *Drp1*$^{\Delta Pax7ER}$ mice increased the levels of proliferating SCs (Ki67$^+$YFP$^+$) in injured muscles, as shown in tissue cryosections (Figure 5F), and rescued the defective muscle regeneration, as shown by increased numbers and sizes of newly formed YFP$^+$ (or eMHC$^+$) myofibers in muscle after injury (Figures 5F and S5E). To exclude secondary effects of DCA, we genetically enhanced OXPHOS by specifically silencing one or all *Pdk* genes in SCs. *Pdk4* is the predominant *Pdk* in SCs (as it expressed ≥ 10 times more than *Pdk1–3* in QSCs) (Figure S5F); its expression drops dramatically upon injury, coinciding with increased OXPHOS metabolism after quiescence exit. We found that *Pdk4* gene silencing alone (Figure S5G) restored the expansion of *Drp1*$^{\Delta Pax7ER}$ SCs following transplantation (Figure 5G) but not fiber size (Figure S5H), whereas silencing all *Pdk* genes (Figure S5G) significantly enhanced YFP$^+$ expansion as well as the myofiber size (Figure 5H). Thus, OXPHOS enhancement, by either pharmacological (DCA treatment) or genetic (silencing *Pdk* genes) approaches, restored the proliferation and regenerative capacity of *Drp1*-null SCs.

We then treated freshly sorted *Drp1*$^{\Delta Pax7ER}$ SCs with rapamycin to induce autophagy (Mammucari et al., 2007; García-Prat et al., 2016), labeled them with DiI, and transplanted them into preinjured, regenerating muscle of immunodeficient recipient mice. Indeed, rapamycin pretreatment significantly restored the expansion and engraftment of these mitochondrial-fission-deficient SCs after transplantation (Figure 5I).

Restoring OXPHOS and mitophagy rescues the regenerative failure of the fission-impaired, physiologically aged satellite cells

Similar to young *Drp1*-null SCs, SCs from old (24–28 month) WT mice also showed functional defects, including reduced proliferation, impaired mitophagy, increased ROS accumulation, and reduced oxidative metabolism, as compared with those from young (2.5–3months) mice (Figures S6A–S6E). This correlated with defective muscle regeneration in old mice after injury (Figure S6F), as expected (see reviews by Evano and Tajbakhsh, 2018; Galliot et al., 2017; Sousa-Victor et al., 2020; Hong et al., 2022; Sousa-Victor et al., 2022), suggesting that SCs with genetic mitochondrial fission impairments undergo a form of premature aging. A comparative bioinformatic analysis of RNA-seq data confirmed that pathways related to mitosis, cell cycle, and mitochondrial metabolism were commonly downregulated in 1DPI-SCs from both old WT mice and young *Drp1*$^{\Delta Pax7ER}$ mice (Figure 6A). Moreover, pathways related to proliferation, mitochondria organization, and several metabolic pathways were further downregulated in 3DPI-SCs from both old WT mice and young *Drp1*$^{\Delta Pax7ER}$ mice (Figure S6G), consistent with their common impaired mitochondrial OXPHOS reprogramming and proliferative capacities.

We thus hypothesized that mitochondrial dynamics are altered with aging, thereby impeding SC metabolic and regenerative functions. At the peak of proliferation (3DPI-SCs), the level of DRP1 was significantly reduced in Pax7$^+$ SCs in the injured old muscle as compared with injured young muscle (Figure 6B). Moreover, both total DRP1 and activated pDRP1 (i.e., phosphorylated at serine residue S579 in mice, which is equivalent to residue S616 in humans) were reduced in SCs from old mice as compared with young ones (Figure 6C). Consistent with this, old SCs showed a higher number of large mitochondria with a higher average volume than young ones (Figures 6D and S6H), indicating that, with aging, SCs remodel their mitochondria after muscle injury with an abnormal shift toward fusion, due to the reduced DRP1 activity. In biopsies of human tissues, SCs with high levels of active DRP1 were found in areas of damaged muscle but not in areas of intact muscle (Figure S6I), confirming that mitochondrial fission activity increases also in the SCs of human muscle after damage/during regeneration. Further, as in mice, SCs from elderly persons showed reduced DRP1 activity compared with those from young adults, consistent with their reduced proliferative potential (Figures S6J–S6L). Thus, fission activity is specifically induced in SCs after muscle damage, but this activity is reduced in old age in both humans and mice.

We then directly increased DRP1 expression in aged SCs using a lentiviral vector (LV) expressing DRP1 under a phosphoglycerate

Figure 4. Mitochondrial fission deficiency impairs mitophagy in satellite cells

Representative images from *Drp1*^{WT} or *Drp1*$^{\Delta Pax7ER}$ satellite cells showing the following:

(A) ROS (CellRox) and mitochondria (left); quantification of total ROS puncta (middle); and mitochondria-specific ROS puncta (right), normalized to cell volume (μm^3).

(B) LC3 and mitochondria (left), quantification of total LC3 puncta per cell (upper right), the total flux of LC3 (ΔLC3) (middle), and mitochondria-related flux of LC3 (mito-ΔLC3) (lower right) after 4 h of treatment with vehicle (veh; DMSO) or bafilomycin A (Baf).

(C) p62 and mitochondria (left), quantification of total p62 puncta (middle), and co-localization of p62 to mitochondria (Mito-p62; right).

(D) Parkin and mitochondria (left), quantification of Parkin signal (IntDen, integrated density; middle), and co-localization of Parkin to mitochondria (Pearson's correlation; right).

Data represent n = 3 mice and are mean ± SD. p values were determined by a two-tailed unpaired t test. Mitochondria were detected with MitoTracker CMX ROS labeling. Scale bars: 3 μm in (A)–(D). See also Figure S4.

CellPress
OPEN ACCESS

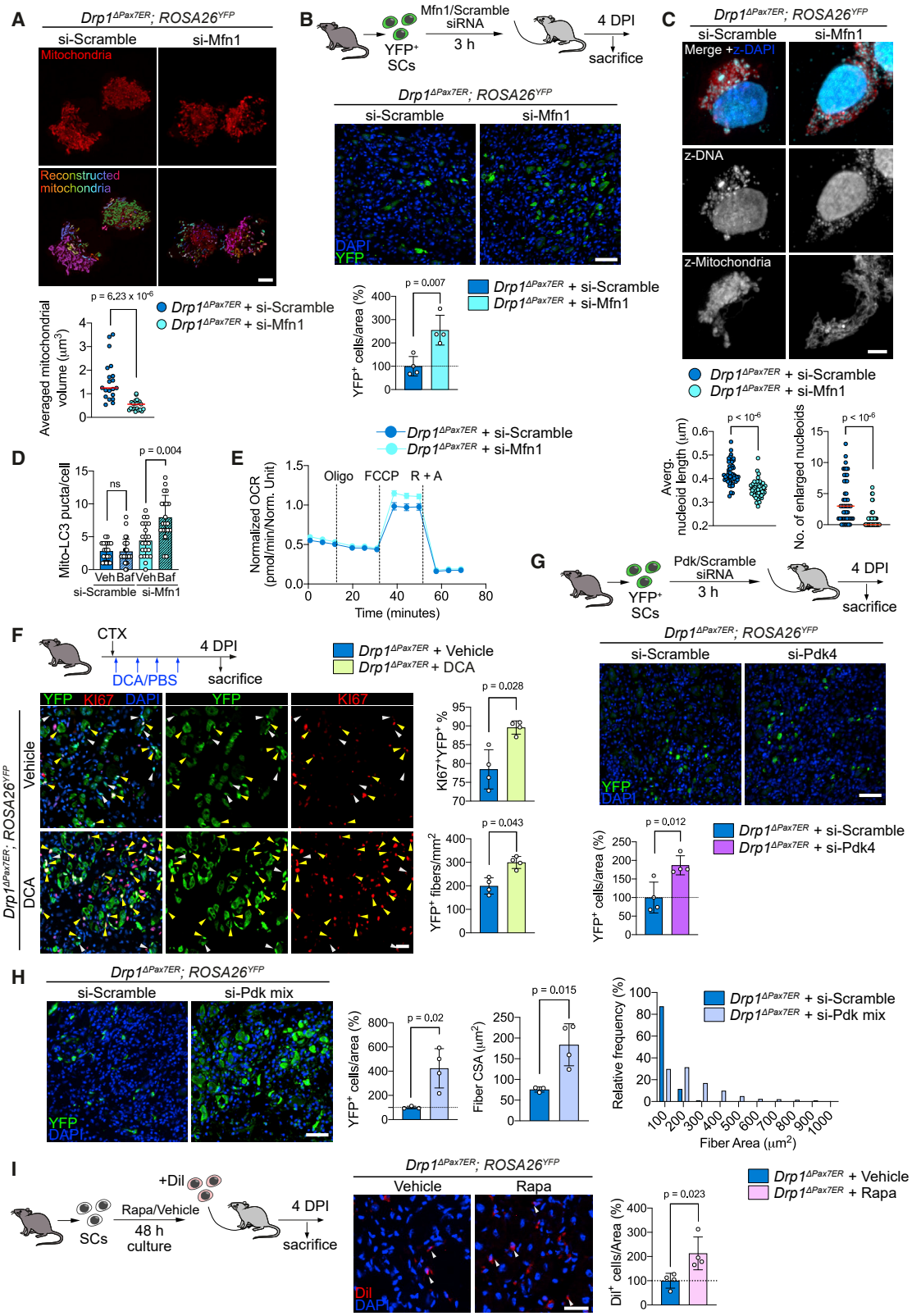

Figure 5. Temporary abrogation of mitochondrial dynamics restores the proliferative capacity of *Drp1*-null satellite cells

(A) Representative images of MitoTracker IF (top) and 3D-reconstructed mitochondrial network (middle) in *Drp1*$^{\Delta Pax7ER}$ satellite cells after *in vitro* si-Scramble or si-Mfn1 treatment and quantification (bottom) of average mitochondrial volume in these cells.

(legend continued on next page)

kinase (PGK) promotor (LV-DRP1). Transduction of this vector into *Drp1*$^{\Delta Pax7ER}$ SCs induced DRP1 protein expression and successfully restored their proliferative capacity (Figures S7A and S7B). Importantly, LV-DRP1 transduction in old SCs improved their engraftment capacity following transplantation in regenerating muscle as compared with control old SCs (e.g., transduced with LV-control) (Figure 6E).

As compared with their young SC counterparts, old QSCs, 1DPI-SCs, and 3DPI-SCs showed reduced expression of all genes involved in ETC complexes (Figure 7A) and had lower mitochondrial respiration (Figure 7B) (see also Pala et al., 2018). This difference reached a maximal level in old 3DPI-SCs, which also showed a significant increase in total and mitochondria-specific ROS levels (Figure 7C). As in young *Drp1*-null SCs, mitophagy was impaired in old SCs (Figures S6C and S6D). Thus, despite having less mitochondrial OXPHOS activity, old SCs accumulated more oxidative damage than young ones after injury, which could be ascribed to the impaired mitophagy and accumulation of defective mitochondria. Furthermore, after muscle damage, old SCs showed an abnormal mtDNA replication: that is, mtDNA copy numbers increased by 10-fold in young 3DPI-SCs but only by 2- to 3-fold in old 3DPI-SCs (Figure 7D). These findings further show that the molecular, cellular, and functional alterations of physiologically aged WT SCs are comparable with those of young *Drp1*-null SCs and reinforce the notions that (1) young *Drp1*-null SCs show premature aging and (2) the decline in mitochondrial fission activity in old SCs may trigger their regenerative deficits.

We next searched for hallmarks of aging in young *Drp1*-null SCs and old WT SCs that could further explain their dysfunction by comparing their transcriptomes with those of old tissues from various species (including humans) (Benayoun et al., 2019; Shavlakadze et al., 2019; Stegeman and Weake, 2017). Common to all was the downregulation of OXPHOS and cell-cycle-related pathways, such as the G2/M cell-cycle checkpoint and E2F and MYC signaling (Figure S7C), which is consistent with multiple previously published transcriptional datasets of aging human, rodent, and killifish (Benayoun et al., 2019; Shavlakadze et al., 2019; Stegeman and Weake, 2017). Notably, unlike old WT SCs, young *Drp1*$^{\Delta Pax7ER}$ SCs did not reveal signs of exacerbated inflammation, which is another hallmark of aging (Figure S7C). Thus, young *Drp1*-null SCs exhibited some (but not all) specific hallmarks of aging, in particular the downregulation of metabolic/mitochondrial and proliferative pathways. Old SCs exhibited the most hallmarks of aging, including age-associated inflammation (inflammaging) (Franceschi and Campisi, 2014), particularly at the 3-DPI proliferative stage, which in turn could add to their reduced regenerative potential.

DCA treatment of old WT mice enhanced the regenerative capacity of SCs in injured muscles as shown by increased numbers of PAX7$^+$/EdU$^+$ SCs in tissue cryosections (Figure 7E) and rescued the defective muscle regeneration (as shown by the increased numbers and sizes of newly formed eMHC$^+$ myofibers after injury) (Figures 7F and S7D). Moreover, silencing all *Pdk* genes in old SCs significantly increased the engraftment of these cells upon transplantation into regenerating muscle, as shown by the higher number of Dil$^+$ cells in the damaged muscle area (Figure 7G), suggesting an improved stem cell proliferation potential. We conclude that OXPHOS enhancement by DCA treatment or *Pdk* silencing improves muscle regeneration upon proliferative failure due to defective mitochondrial fission in SCs, both for physiologically impaired old cells and for young cells with genetic loss of mitochondrial fission.

We next investigated whether enhancing either autophagy or mitophagy could rescue the regenerative defects of these cells. Rapamycin pretreatment significantly restored the expansion and engraftment of old SCs after transplantation, as shown by the higher number of Dil$^+$ SCs in the regenerating muscles of the recipient mice (Figure 7H), in agreement with previous findings (García-Prat et al., 2016). Likewise, treatment with the natural mitophagy inducer urolithin A (Liu et al., 2022; Luan et al., 2021; Ryu et al., 2016) enhanced the number of proliferating

(B) Schematics of transplantation of satellite cells from *Drp1*$^{\Delta Pax7ER}$ mice after *ex vivo Mfn1* siRNA silencing or scramble treatment (top) into preinjured muscles of immunodeficient mice. Representative images of transplanted muscle sections are shown of YFP and DAPI (middle) and quantification (bottom) of YFP$^+$ cells per area.

(C) Representative IF images of DNA and mitochondria (top) as well as quantification of nucleoid size by average mitochondrial nucleoid length (lower left) and number of extremely large nucleoids (length > 0.8 μm; lower right) in *Drp1*$^{\Delta Pax7ER}$ proliferating satellite cells after *ex vivo* si-Scramble or si-Mfn1 treatment.

(D) Quantification of LC3-mitochondria co-localization in *Drp1*$^{\Delta Pax7ER}$ satellite cells after *ex vivo* si-Scramble or si-Mfn1 treatment, followed by 4 h of treatment with vehicle (DMSO) or bafilomycin A (Baf).

(E) Normalized oxygen-consumption rates (OCRs) of *Drp1*$^{\Delta Pax7ER}$ satellite cells after *ex vivo* si-Scramble or si-*Mfn1* treatment at baseline and in response to oligomycin A (oligo), FCCP, or rotenone plus antimycin A (R + A). Data were obtained using Seahorse XF96 and normalized to protein level using CyQUANT cell-proliferation assay.

(F) Schematics of DCA and vehicle (PBS) application after CTX injury (upper left) and representative IF images of YFP, KI67, and DAPI staining in muscles of *Drp1*$^{\Delta Pax7ER}$ mice (± DCA treatment) at 4 DPI (lower left). Quantification of the percentage of KI67$^+$ cells to total YFP$^+$ cells (upper right) and the number of YFP$^+$ fibers per mm^2 damaged muscle area (lower right).

(G) Schematics of transplantation of satellite cells from *Drp1*$^{\Delta Pax7ER}$ mice after *ex vivo Pdk* siRNA silencing or scramble treatment (top) into preinjured muscles of immunodeficient mice. Representative images of transplanted muscle sections are shown of YFP and DAPI (middle) and quantification (bottom) of YFP$^+$ cells per area.

(H) Representative images of transplanted muscle sections are shown of YFP and DAPI (left) and quantification (right) of YFP$^+$ cells per area, median CSA of YFP$^+$ fibers and YFP$^+$ fiber-size distribution in samples transplanted with satellite cells from *Drp1*$^{\Delta Pax7ER}$ mice after mixed *Pdk*1-4 siRNA or scramble treatment. For schematics, see (G).

(I) Schematics of transplantation of satellite cells from *Drp1*$^{\Delta Pax7ER}$ mice after *ex vivo* rapamycin (or vehicle) treatment (left) into preinjured muscles of immunodeficient mice. Representative images of transplanted muscle sections are shown of Dil and DAPI (middle) and quantification (right) of Dil$^+$ cells per area.

Data represent n = 3–4 mice and are mean ± SD. p values were determined by a two-tailed unpaired t test. Mitochondria were labeled with MitoTracker CMX ROS in (A) and (C). Data were analyzed at 4 DPI post-transplantation in (C), (G), (H), and (I), and the values presented are relative to the level of control (si-Scramble- or vehicle-treated group). Scale bars: 3 μm in (A) and (C) and 25 μm in (B), (F), (G), (H), and (I). See also Figure S5.

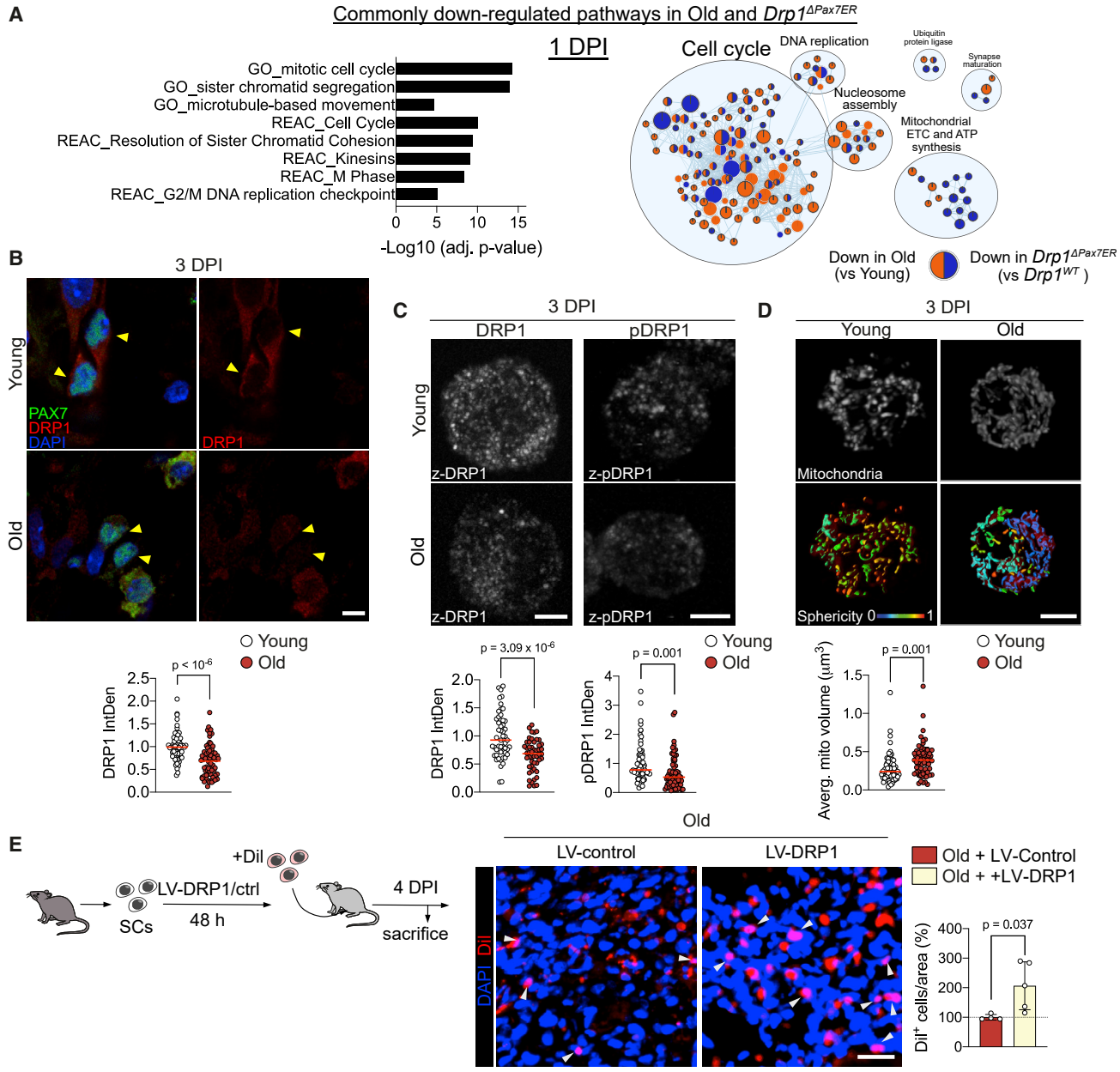

Figure 6. Impaired mitochondrial fission causes regenerative failure in old satellite cells

(A) Commonly altered pathways detected in young versus old mouse 1DPI-SCs and in *Drp1*^{WT} versus *Drp1*$^{\Delta Pax7ER}$ datasets. Commonly altered DE genes were analyzed in g:Profiler. The top gene ontology (GO), Reactome, and Kyoto Encyclopedia of Genes and Genomes (KEGG) pathways are shown (left). Enrichment map of common pathway clusters enriched in old or *Drp1*$^{\Delta Pax7ER}$ 1DPI-SCs. Orange nodes represent pathways downregulated in old versus young 1DPI-SCs (FDR < 0.25); blue nodes represent pathways downregulated in *Drp1*$^{\Delta Pax7ER}$ versus *Drp1*^{WT} 1DPI-SCs.

(B) Representative IF images of PAX7, DRP1, and DAPI staining (top), and quantification of DRP1 signal of young and old 3-DPI TA muscles (bottom).

(C) Representative IF images of total and active DRP1 (pDRP, phosphorylated DRP1) staining (top) and quantification of DRP1 (lower left) and pDRP (lower right) signals in 3DPI-SCs from young or old mice.

(D) Representative images of MitoTracker (top, upper panel) and 3D-reconstructed mitochondrial network (top, lower panel) in 3DPI-SCs from young or old mice and quantification of average mitochondrial volume in each cell (bottom). Reconstructed mitochondria were colored based on their sphericity (0–1).

(E) Schematics of transplantation of satellite cells from old mice after *ex vivo* DRP1 or control lentiviral vector transduction (left) into preinjured muscles of immunodeficient mice. Representative images are shown of Dil and DAPI (middle) and quantification (right) of Dil^{+} cells per area. Data were analyzed at 4 DPI post-transplantation. The values presented are relative to the level of control (LV-control-treated group).

Data represent n = 3–4 mice and are mean ± SD. p values were determined by a two-tailed unpaired t test. IntDen, integrated density. Scale bars: 5 μm in (B), 3 μm in (C) and (D), and 25 μm in (E). See also Figure S6 and Table S3.

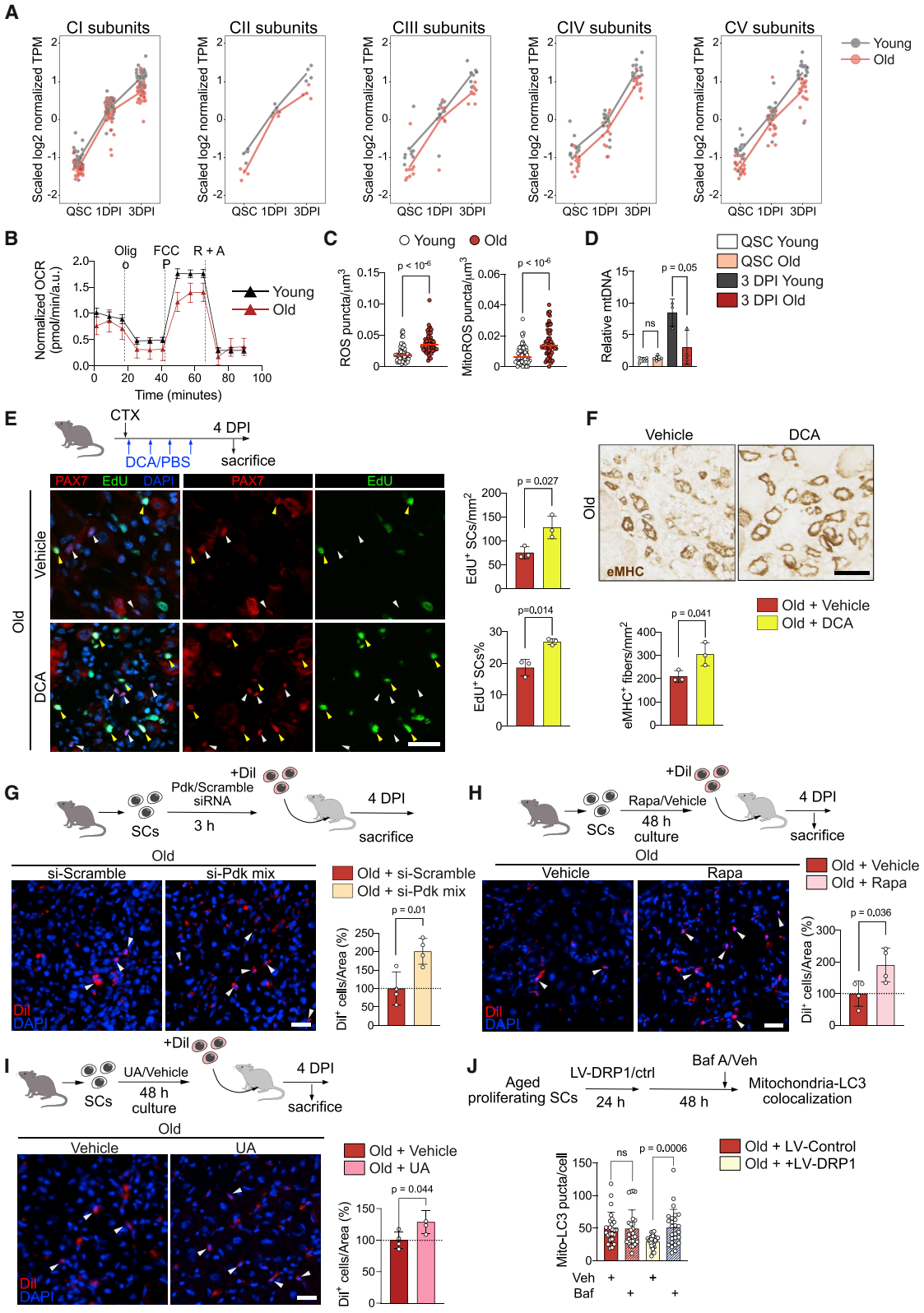

(legend on next page)

old SCs after engraftment (Figure 7I). Furthermore, LV-DRP1 transduction enhanced the mitophagic flux in old SCs, as shown by less LC3 accumulation (Figure 7J), suggesting that enhanced functionality of old SCs by DRP1 re-expression may be at least partially ascribed to mitophagy reinduction.

In sum, the detrimental functional consequences of impaired mitochondrial fission in SCs, which occurs during aging or after complete ablation of the *Drp1* gene, can be overcome by reinducing mitochondrial metabolism and mitophagy, as well as by direct DRP1 expression (see Figure S7E).

DISCUSSION

The regenerative capacity of stem cells declines with aging. Our data illustrate that SCs of young-adult skeletal muscle require complex mitochondria physical remodeling after tissue injury to meet the regenerative demands—namely, they must rapidly expand and generate sufficient stem cell progeny to form new myofibers to replace damaged tissue. Conversely, inadequate mitochondria remodeling compromises regeneration, and this occurs in the old muscle. We propose that mitochondria morphology and function are tightly interconnected in stem cells and that this connection is critical in the switch between quiescence and the proliferative fate of these cells during tissue repair. Our findings point to a model in which mitochondrial fission is indispensable for providing sufficient stem cell progeny during the regeneration process, by governing two major activities: mitochondrial OXPHOS and mitophagy (Figure S7E). This fission mechanism fails in advanced aging.

Mitochondria dynamics determine mtDNA distribution and transmission, as well the structure of the cristae and mitochondrial segregation and elimination. Therefore, alteration of mitochondria dynamics directly impacts OXPHOS function at multiple levels: (1) it affects the balanced synthesis and assembly of the mtDNA encoded proteins (reviewed in the study conducted by Busch et al., 2014); (2) it disturbs proper quality control of mitochondria by mitophagy (Twig et al., 2008); and (3) it impacts the structural organization of the ETC (Balsa et al., 2019; Cogliati et al., 2013). Here we show that, unlike young/fit SCs, aged SCs (as well as those genetically impaired for mitochondrial fission) present: (1) quantitative deregulation of most mitochondrial ETC subunits, (2) impaired mtDNA replication, and (3) an aberrant presence of nucleoids. Together, these mitochondrial abnormalities underpin the low efficiency of the ETC and OXPHOS, which are critical functions for the satellite cell proliferative phase after tissue injury. SCs were also incapable of removing damaged mitochondria when fission was impaired, due to depressed mitophagy, thereby provoking excessive ROS (Figure S7E). Thus, we propose that mitochondrial fission is a decisive factor in the switch between quiescence and the proliferative fate of muscle stem cells during regeneration, by governing metabolism and proteostasis. Restoration of mitochondrial fission (by directly increasing DRP1 levels) or provoking mitochondrial adynamism through mitochondrial fusion blockade (by silencing the fusion regulator *Mfn1*) enhances the proliferative capacity of $Drp1^{\Delta Pax7ER}$ SCs as well as of normally aged SCs, correlating with enhanced mitochondrial respiratory capacity and mitophagy. Of note, we also observed signs of reduced mitochondrial fission that correlate with deficient cell functions in human SCs from aged humans; notably, these cells also showed impaired autophagy (García-Prat et al., 2016). Thus, this fission regulatory mechanism is also likely to deteriorate in human SCs during aging.

Although aging-induced stem cell regenerative decline is often viewed as an irreversible process, we provide evidence that *in vivo* enhancement of either OXPHOS or autophagy (and even by directly manipulating mitochondrial dynamics), rejuvenates SCs and surmounts their mitochondrial fission and functional failure. Conceptually, these findings suggest that the intrinsic hallmarks of aging in stem cells (such as the ones we identified here) can be pharmacologically manipulated to achieve better regeneration in human sarcopenia.

Limitations of the study

We addressed several technical limitations to measuring metabolic parameters of truly quiescent SCs. For instance, obtaining viable cells for metabolic analyses inflict an undetermined degree of stress on cells. Thus, we used freshly sorted SCs that were maintained in a hypoxia chamber for 6 h before measuring mitochondrial respiration with the Seahorse analysis (a protocol adapted from Pala et al., 2018). However, the culture interval might compromise the maintenance of the true quiescence state of the cells. Additionally, only old female mice were used, due to the limited availability of old male mice; further studies

Figure 7. Restoring OXPHOS and mitophagy rescues the regenerative failure of the fission-impaired physiological-aged satellite cells

(A) *Z* score analysis of ETC complex I–V genes throughout analyzed states in young or old satellite cells, presented in dot graph.

(B) Normalized OCR of 48-h cultured young or old satellite cells at baseline and in response to oligomycin A (oligo), FCCP, or rotenone plus antimycin A (R + A). Data were obtained using Seahorse XF96 and normalized to protein levels using CyQUANT cell-proliferation assay.

(C) Quantification of total (left) and mitochondrial (right) ROS (CellRox) in young or old 3DPI-SCs.

(D) Quantification of mtDNA copy numbers relative to young QSC levels. mtDNA copy numbers were normalized to genomic DNA copy numbers, as quantified by qPCR ($2^{-\Delta CT}$).

(E) Schematics of DCA/vehicle (PBS) treatment scheme in old mice and representative images of PAX7, EdU, and DAPI IF staining in old muscle (± DCA treatment) at 4 DPI (left), and quantification of EdU^+ satellite cells per mm^2 injured area (upper right) and percentage of EdU^+ SCs (lower right).

(F) Representative images of regenerating fibers, identified by eMHC IHC (left), and number of $eMHC^+$ fibers from (E).

(G–I) Schematics (top) of transplantation of satellite cells from old mice into preinjured muscles of immunodeficient mice after *ex vivo* treatment of siPdk4 versus scramble (G), rapamycin (Rapa) versus vehicle (H), or urolithin A (UA) versus vehicle (I). Representative images are shown of Dil and DAPI (lower left) and quantification (lower right) of Dil^+ cells per area. Data were analyzed at 4 DPI post-transplantation. Values are relative to the level of control (si-Scramble- or vehicle-treated group).

(J) Schematics of *ex vivo* LV-DPR1 or LV-control transduction of satellite cells followed by 4 h of treatment with vehicle (veh, DMSO) or bafilomycin A (Baf) (top) and quantification of LC3-mitochondria co-localization (bottom).

Data represent n = 3–5 mice and are mean ± SD. p values were determined by a two-tailed unpaired t test. Scale bars: 25 μm in (E), (G), (H), and (I) and 50 μm in (F). See also Figure S7.

are required to clarify the influence of sex on the aging parameters.

STAR★METHODS

Detailed methods are provided in the online version of this paper and include the following:

- KEY RESOURCES TABLE
- RESOURCE AVAILABILITY
  - Lead contact
  - Materials availability
  - Data and code availability
- EXPERIMENTAL MODEL AND SUBJECT DETAILS
  - Mice
  - Human samples
  - Mouse satellite cell isolation by FACS
  - Primary cell cultures
- METHOD DETAILS
  - Animal procedures
  - Satellite cell transplantation
  - In vivo DCA treatment
  - *Ex vivo* transfection and infection
  - *Ex vivo* analysis of autophagy/mitophagy flux
  - *Ex vivo* DCA treatment
  - Histology and immunohistochemistry (IHC) in muscle cryosections
  - Mitochondrial morphology analysis
  - Proliferation assays
  - ATP content analysis
  - mtDNA quantification
  - Cellular metabolic analysis
  - Flow cytometry assays
  - CellRox assay
  - RT-qPCR
  - Western blotting
  - Transmission electron microscopy
  - RNA-seq sample and library preparation
  - Bulk RNA-seq Data Pre-processing
  - Differential gene expression and pathway enrichment analysis
  - Gene Set Enrichment Analysis (GSEA) and Cytoscape
  - Comparative enrichment analysis using previously published aging dataset
- QUANTIFICATION AND STATISTICAL ANALYSIS
  - Digital image acquisition and analysis
  - Image analysis
  - Statistical analysis

SUPPLEMENTAL INFORMATION

Supplemental information can be found online at https://doi.org/10.1016/j.stem.2022.07.009.

ACKNOWLEDGMENTS

We thank J. M. Ballesteros, L. Ortet, V. Lukesova, E. Andrés, V. Moiseeva, A. Navarro, and M. Raya for their technical contributions, L. García-Prat for initiating satellite cell/mitophagy studies, and all members of the P.M.C. laboratory for their helpful discussions. We are very grateful to L. Scorrano for the *Drp1*-floxed (and *Opa1*-floxed) mouse lines and for reading the manuscript, V. Romanello for help in obtaining mouse lines, F. Sánchez-Cabo and M. J. Gómez for assistance in bioinformatics, and R.I. Klein Geltink and E. Pearce for advice on 3D mitochondria analysis; we also thank M.B. Alvarez-Flores and E. Prieto-García (CNIC FACS Facility); V. Caiolfa and V. Labrador-Cantarero (CNIC Advanced Microscopy Facility); A. Dopazo and A. Benguria (CNIC-Genomics Facility); S. Rodríguez-Colilla (CNIC-Animal Facility); and Myoage network and tissue bank and Hospital Vall d'Hebron, for human material. We are also indebted to Veronica Raker for excellent editing. Work in the PMC laboratory was supported by Spanish Ministerio de Ciencia e Innovación (RTI2018-096068 to P.M.-C. and E.P), ERC-2016-AdG-741966, LaCaixa-HEALTH-HR17-00040, MDA, UPGRADE-H2020-825825, AFM-Telethon, DPP-Spain, Fundació La Marató TV3-80/19-202021 to P.M.-C; Fundació La Marató TV3-137/38-202033 to A.L.S.; partly supported by Milky Way Research Foundation (MWRF) to P.M.-C; Severo Ochoa Program for Centers of Excellence to CNIC (SEV-2015-0505) and Maria de Maeztu Program for Units of Excellence to UPF (MDM-2014-0370). Work in the JAE laboratory was supported by Ministerio de Ciencia e Innovacion (RTI2018-099357-B-I00, RED2018-102576-T), Human Frontier Science Program HFSP (RGP0016/2018), Centro de Investigación Biomédica en Red en Fragilidad y Envejecimento Saludable (CIBERFES16/10/00282), and Leduq Foundation award (REDOX-17CVD04). Work in JMV laboratory was supported by the Spanish Ministerio de Ciencia e Innovación (RTI2018-100695-B-I00), Spanish Junta de Andalucía (P18-RT-4264, 1263735-R and BIO-276), the FEDER Funding Program from the European Union, and Universidad de Córdoba. The authors are indebted to the personnel from the Servicio Centralizado de Apoyo a la Investigación (SCAI; University of Córdoba) for technical support with the transmission electron microscope. Work in MS laboratory was funded by the Italian Assoc. for Cancer Research (AIRC IG-D17388 and ID23257) and ASI (MARS-PRE, project DC-VUM-2017-006). X.H., S.C., I.R.-P, and A.C were supported by Severo Ochoa PFI, PI, FPI, and H2020 Marie Skłodowska-Curie Actions predoctoral fellowships, respectively. P.H.-A was supported by Juan de la Cierva-Incorporación fellowship.

AUTHOR CONTRIBUTIONS

Conceptualization, P.M.-C., X.H., J.I., and J.A.E. Formal analysis, X.H., O.D., and J.I. Investigation, X.H., S.C., I.R.-P., J.S., P.H.-A., A.C., A.P., J.A.G.-R., J.M.V., and A.L.S. Writing—original draft, P.M.-C., X.H., J.I., and J.A.E. Writing—review & editing, P.M.-C., X.H., E.P., J.I., and J.A.E. Funding acquisition, P.M.-C. Resources, M.S. Visualization, X.H., E.P., J.A.E., and J.I. Supervision, P.M.-C., J.I., and J.A.E.

DECLARATION OF INTERESTS

The authors declare no competing interests.

Received: September 1, 2021
Revised: June 9, 2022
Accepted: July 22, 2022
Published: August 22, 2022; corrected online: August 26, 2022

REFERENCES

Adebayo, M., Singh, S., Singh, A.P., and Dasgupta, S. (2021). Mitochondrial fusion and fission: the fine-tune balance for cellular homeostasis. FASEB J. *35*, e21620.

Balsa, E., Soustek, M.S., Thomas, A., Cogliati, S., García-Poyatos, C., Martín-García, E., Jedrychowski, M., Gygi, S.P., Enriquez, J.A., and Puigserver, P. (2019). ER and nutrient stress promote assembly of respiratory chain supercomplexes through the PERK-eIF2α axis. Mol. Cell *74*, 877–890.e6.

Benayoun, B.A., Pollina, E.A., Singh, P.P., Mahmoudi, S., Harel, I., Casey, K.M., Dulken, B.W., Kundaje, A., and Brunet, A. (2019). Remodeling of epigenome and transcriptome landscapes with aging in mice reveals widespread induction of inflammatory responses. Genome Res. *29*, 697–709.

Busch, K.B., Kowald, A., and Spelbrink, J.N. (2014). Quality matters: how does mitochondrial network dynamics and quality control impact on mtDNA integrity? Philos. Trans. R. Soc. Lond. B Biol. Sci. *369*, 20130442.

Chan, D.C. (2012). Fusion and fission: interlinked processes critical for mitochondrial health. Annu. Rev. Genet. *46*, 265–287.

Chandel, N.S., Jasper, H., Ho, T.T., and Passegué, E. (2016). Metabolic regulation of stem cell function in tissue homeostasis and organismal ageing. Nat. Cell Biol. *18*, 823–832.

Cogliati, S., Frezza, C., Soriano, M.E., Varanita, T., Quintana-Cabrera, R., Corrado, M., Cipolat, S., Costa, V., Casarin, A., Gomes, L.C., et al. (2013). Mitochondrial cristae shape determines respiratory chain supercomplexes assembly and respiratory efficiency. Cell *155*, 160–171.

Corrado, M., Samardžić, D., Giacomello, M., Rana, N., Pearce, E.L., and Scorrano, L. (2021). Deletion of the mitochondria-shaping protein Opa1 during early thymocyte maturation impacts mature memory T cell metabolism. Cell Death Differ. *28*, 2194–2206.

Cunningham, F., Amode, M.R., Barrell, D., Beal, K., Billis, K., Brent, S., Carvalho-Silva, D., Clapham, P., Coates, G., Fitzgerald, S., et al. (2015). Ensembl 2015. Nucleic Acids Res. *43*, D662–D669.

Detmer, S.A., and Chan, D.C. (2007). Functions and dysfunctions of mitochondrial dynamics. Nat. Rev. Mol. Cell Biol. *8*, 870–879.

Djalalvandi, A., and Scorrano, L. (2022). Mitochondrial dynamics: roles in exercise physiology and muscle mass regulation. Curr. Opin. Physiol. *27*, 100550.

Duchen, M.R. (2000). Mitochondria and calcium: from cell signalling to cell death. J. Physiol. *529*, 57–68.

El Fissi, N., Rojo, M., Aouane, A., Karatas, E., Poliacikova, G., David, C., Royet, J., and Rival, T. (2018). Mitofusin gain and loss of function drive pathogenesis in *Drosophila* models of CMT 2A neuropathy. EMBO Rep. *19*, e45241.

Evano, B., and Tajbakhsh, S. (2018). Skeletal muscle stem cells in comfort and stress. npj Regen. Med. *3*, 24.

Farge, G., Mehmedovic, M., Baclayon, M., van den Wildenberg, S.M.J.L., Roos, W.H., Gustafsson, C.M., Wuite, G.J.L., and Falkenberg, M. (2014). In vitro-reconstituted nucleoids can block mitochondrial DNA replication and transcription. Cell Rep. *8*, 66–74.

Franceschi, C., and Campisi, J. (2014). Chronic inflammation (inflammaging) and its potential contribution to age-associated diseases. J. Gerontol. A Biol. Sci. Med. Sci. *69* (*Suppl 1*), S4–S9.

Galliot, B., Crescenzi, M., Jacinto, A., and Tajbakhsh, S. (2017). Trends in tissue repair and regeneration. Development *144*, 357–364.

García-Prat, L., Martínez-Vicente, M., Perdiguero, E., Ortet, L., Rodríguez-Ubreva, J., Rebollo, E., Ruiz-Bonilla, V., Gutarra, S., Ballestar, E., Serrano, A.L., et al. (2016). Autophagy maintains stemness by preventing senescence. Nature *529*, 37–42.

García-Prat, L., Perdiguero, E., Alonso-Martín, S., Dell'Orso, S., Ravichandran, S., Brooks, S.R., Juan, A.H., Campanario, S., Jiang, K., Hong, X., et al. (2020a). FoxO maintains a genuine muscle stem-cell quiescent state until geriatric age. Nat. Cell Biol. *22*, 1307–1318.

García-Prat, L., Sousa-Victor, P., and Muñoz-Cánoves, P. (2017). Proteostatic and metabolic control of stemness. Cell Stem Cell *20*, 593–608.

Giacomello, M., Pyakurel, A., Glytsou, C., and Scorrano, L. (2020). The cell biology of mitochondrial membrane dynamics. Nat. Rev. Mol. Cell Biol. *21*, 204–224.

Giorgi, C., Marchi, S., and Pinton, P. (2018). The machineries, regulation and cellular functions of mitochondrial calcium. Nat. Rev. Mol. Cell Biol. *19*, 713–730.

Hamanaka, R.B., and Chandel, N.S. (2010). Mitochondrial reactive oxygen species regulate cellular signaling and dictate biological outcomes. Trends Biochem. Sci. *35*, 505–513.

Hockenbery, D., Nuñez, G., Milliman, C., Schreiber, R.D., and Korsmeyer, S.J. (1990). Bcl-2 is an inner mitochondrial membrane protein that blocks programmed cell death. Nature *348*, 334–336.

Hong, X., Campanario, S., Ramírez-Pardo, I., Grima-Terrén, M., Isern, J., and Muñoz-Cánoves, P. (2022). Stem cell aging in the skeletal muscle: the importance of communication. Ageing Res. Rev. *73*, 101528.

Ishihara, T., Ban-Ishihara, R., Maeda, M., Matsunaga, Y., Ichimura, A., Kyogoku, S., Aoki, H., Katada, S., Nakada, K., Nomura, M., et al. (2015). Dynamics of mitochondrial DNA nucleoids regulated by mitochondrial fission is essential for maintenance of homogeneously active mitochondria during neonatal heart development. Mol. Cell. Biol. *35*, 211–223.

Ishihara, N., Nomura, M., Jofuku, A., Kato, H., Suzuki, S.O., Masuda, K., Otera, H., Nakanishi, Y., Nonaka, I., Goto, Y., et al. (2009). Mitochondrial fission factor Drp1 is essential for embryonic development and synapse formation in mice. Nat. Cell Biol. *11*, 958–966.

Jassal, B., Matthews, L., Viteri, G., Gong, C., Lorente, P., Fabregat, A., Sidiropoulos, K., Cook, J., Gillespie, M., Haw, R., et al. (2020). The reactome pathway knowledgebase. Nucleic Acids Res. *48*, D498–D503.

John, G.B., Shang, Y., Li, L., Renken, C., Mannella, C.A., Selker, J.M.L., Rangell, L., Bennett, M.J., and Zha, J. (2005). The mitochondrial inner membrane protein mitofilin controls cristae morphology. Mol. Biol. Cell *16*, 1543–1554.

Kucera, M., Isserlin, R., Arkhangorodsky, A., and Bader, G.D. (2016). AutoAnnotate: a cytoscape app for summarizing networks with semantic annotations. F1000Res *5*, 1717.

Kuroda, Y., Sako, W., Goto, S., Sawada, T., Uchida, D., Izumi, Y., Takahashi, T., Kagawa, N., Matsumoto, M., Matsumoto, M., et al. (2012). Parkin interacts with Klokin1 for mitochondrial import and maintenance of membrane potential. Hum. Mol. Genet. *21*, 991–1003.

Le, G., Lowe, D.A., and Kyba, M. (2016). Freeze injury of the tibialis anterior muscle. Methods Mol. Biol. *1460*, 33–41.

Li, B., and Dewey, C.N. (2011). RSEM: accurate transcript quantification from RNA-seq data with or without a reference genome. BMC Bioinformatics *12*, 323.

Li, H., Ruan, Y., Zhang, K., Jian, F., Hu, C., Miao, L., Gong, L., Sun, L., Zhang, X., Chen, S., et al. (2016). Mic60/Mitofilin determines MICOS assembly essential for mitochondrial dynamics and mtDNA nucleoid organization. Cell Death Differ. *23*, 380–392.

Liaghati, A., Pileggi, C.A., Parmar, G., Patten, D.A., Hadzimustafic, N., Cuillerier, A., Menzies, K.J., Burelle, Y., and Harper, M.-E. (2021). Grx2 regulates skeletal muscle mitochondrial structure and autophagy. Front. Physiol. *12*, 604210.

Liberzon, A., Subramanian, A., Pinchback, R., Thorvaldsdóttir, H., Tamayo, P., and Mesirov, J.P. (2011). Molecular signatures database (MSigDB) 3.0. Bioinformatics *27*, 1739–1740.

Liu, S., D'Amico, D., Shankland, E., Bhayana, S., Garcia, J.M., Aebischer, P., Rinsch, C., Singh, A., and Marcinek, D.J. (2022). Effect of urolithin A supplementation on muscle endurance and mitochondrial health in older adults: a randomized clinical trial. JAMA Netw. Open *5*, e2144279.

Liu, X., Kim, C.N., Yang, J., Jemmerson, R., and Wang, X. (1996). Induction of apoptotic program in cell-free extracts: requirement for dATP and cytochrome c. Cell *86*, 147–157.

Love, M.I., Huber, W., and Anders, S. (2014). Moderated estimation of fold change and dispersion for RNA-seq data with DESeq2. Genome Biol. *15*, 550.

Luan, P., D'Amico, D., Andreux, P.A., Laurila, P.-P., Wohlwend, M., Li, H., Imamura de Lima, T., Place, N., Rinsch, C., Zanou, N., and Auwerx, J. (2021). Urolithin A improves muscle function by inducing mitophagy in muscular dystrophy. Sci. Transl. Med. *13*, eabb0319.

Mammucari, C., Milan, G., Romanello, V., Masiero, E., Rudolf, R., Del Piccolo, P., Burden, S.J., Di Lisi, R., Sandri, C., Zhao, J., et al. (2007). FoxO3 controls autophagy in skeletal muscle in vivo. Cell Metab. *6*, 458–471.

Martin, M. (2011). Cutadapt removes adapter sequences from high-throughput sequencing reads. EMBnet J. *17*, 10.

Matsuda, N., Sato, S., Shiba, K., Okatsu, K., Saisho, K., Gautier, C.A., Sou, Y.S., Saiki, S., Kawajiri, S., Sato, F., et al. (2010). PINK1 stabilized by mitochondrial depolarization recruits Parkin to damaged mitochondria and activates latent Parkin for mitophagy. J. Cell Biol. *189*, 211–221.

Merico, D., Isserlin, R., Stueker, O., Emili, A., and Bader, G.D. (2010). Enrichment map: a network-based method for gene-set enrichment visualization and interpretation. PLoS One *5*, e13984.

Narendra, D., Tanaka, A., Suen, D.-F., and Youle, R.J. (2008). Parkin is recruited selectively to impaired mitochondria and promotes their autophagy. J. Cell Biol. *183*, 795–803.

Nishijo, K., Hosoyama, T., Bjornson, C.R.R., Schaffer, B.S., Prajapati, S.I., Bahadur, A.N., Hansen, M.S., Blandford, M.C., McCleish, A.T., Rubin, B.P., et al. (2009). Biomarker system for studying muscle, stem cells, and cancer in vivo. FASEB J. *23*, 2681–2690.

Okatsu, K., Oka, T., Iguchi, M., Imamura, K., Kosako, H., Tani, N., Kimura, M., Go, E., Koyano, F., Funayama, M., et al. (2012). PINK1 autophosphorylation upon membrane potential dissipation is essential for Parkin recruitment to damaged mitochondria. Nat. Commun. *3*, 1016.

Pala, F., Di Girolamo, D., Mella, S., Yennek, S., Chatre, L., Ricchetti, M., and Tajbakhsh, S. (2018). Distinct metabolic states govern skeletal muscle stem cell fates during prenatal and postnatal myogenesis. J. Cell Sci. *131*, jcs212977.

Parone, P.A., Da Cruz, S., Tondera, D., Mattenberger, Y., James, D.I., Maechler, P., Barja, F., and Martinou, J.-C. (2008). Preventing mitochondrial fission impairs mitochondrial function and leads to loss of mitochondrial DNA. PLoS One *3*, e3257.

Perdiguero, E., Sousa-Victor, P., Ruiz-Bonilla, V., Jardí, M., Caelles, C., Serrano, A.L., and Muñoz-Cánoves, P. (2011). MKP-1-regulated AKT coordinates macrophage transitions and resolution of inflammation during tissue repair. J. Cell Biol. *195*, 307–322.

Rambold, A.S., and Pearce, E.L. (2018). Mitochondrial dynamics at the interface of immune cell metabolism and function. Trends Immunol. *39*, 6–18.

Raudvere, U., Kolberg, L., Kuzmin, I., Arak, T., Adler, P., Peterson, H., and Vilo, J. (2019). g:profiler: a web server for functional enrichment analysis and conversions of gene lists (2019 update). Nucleic Acids Res. *47*, W191–W198.

Reimand, J., Isserlin, R., Voisin, V., Kucera, M., Tannus-Lopes, C., Rostamianfar, A., Wadi, L., Meyer, M., Wong, J., Xu, C., et al. (2019). Pathway enrichment analysis and visualization of omics data using g:profiler, GSEA, cytoscape and EnrichmentMap. Nat. Protoc. *14*, 482–517.

Ritchie, M.E., Phipson, B., Wu, D., Hu, Y., Law, C.W., Shi, W., and Smyth, G.K. (2015). limma powers differential expression analyses for RNA-sequencing and microarray studies. Nucleic Acids Res. *43*, e47.

Rizzuto, R., De Stefani, D., Raffaello, A., and Mammucari, C. (2012). Mitochondria as sensors and regulators of calcium signalling. Nat. Rev. Mol. Cell Biol. *13*, 566–578.

Robinson, M.D., McCarthy, D.J., and Smyth, G.K. (2010). edgeR: a Bioconductor package for differential expression analysis of digital gene expression data. Bioinformatics *26*, 139–140.

Rocheteau, P., Gayraud-Morel, B., Siegl-Cachedenier, I., Blasco, M.A., and Tajbakhsh, S. (2012). A subpopulation of adult skeletal muscle stem cells retains all template DNA strands after cell division. Cell *148*, 112–125.

Rodgers, J.T., King, K.Y., Brett, J.O., Cromie, M.J., Charville, G.W., Maguire, K.K., Brunson, C., Mastey, N., Liu, L., Tsai, C.-R., et al. (2014). mTORC1 controls the adaptive transition of quiescent stem cells from G0 to G(Alert). Nature *510*, 393–396.

Ryall, J.G., Dell'Orso, S., Derfoul, A., Juan, A., Zare, H., Feng, X., Clermont, D., Koulnis, M., Gutierrez-Cruz, G., Fulco, M., and Sartorelli, V. (2015). The NAD^+-dependent SIRT1 deacetylase translates a metabolic switch into regulatory epigenetics in skeletal muscle stem cells. Cell Stem Cell *16*, 171–183.

Ryu, D., Mouchiroud, L., Andreux, P.A., Katsyuba, E., Moullan, N., Nicolet-dit-Félix, A.A., Williams, E.G., Jha, P., Lo Sasso, G., Huzard, D., et al. (2016). Urolithin A induces mitophagy and prolongs lifespan in C. elegans and increases muscle function in rodents. Nat. Med. *22*, 879–888.

Sacco, A., Mourkioti, F., Tran, R., Choi, J., Llewellyn, M., Kraft, P., Shkreli, M., Delp, S., Pomerantz, J.H., Artandi, S.E., and Blau, H.M. (2010). Short telomeres and stem cell exhaustion model Duchenne muscular dystrophy in mdx/mTR mice. Cell *143*, 1059–1071.

Sahu, A., Mamiya, H., Shinde, S.N., Cheikhi, A., Winter, L.L., Vo, N.V., Stolz, D., Roginskaya, V., Tang, W.Y., St Croix, C., et al. (2018). Age-related declines in α-klotho drive progenitor cell mitochondrial dysfunction and impaired muscle regeneration. Nat. Commun. *9*, 4859.

Shadel, G.S., and Horvath, T.L. (2015). Mitochondrial ROS signaling in organismal homeostasis. Cell *163*, 560–569.

Shannon, P., Markiel, A., Ozier, O., Baliga, N.S., Wang, J.T., Ramage, D., Amin, N., Schwikowski, B., and Ideker, T. (2003). Cytoscape: a software environment for integrated models of biomolecular interaction networks. Genome Res. *13*, 2498–2504.

Shavlakadze, T., Morris, M., Fang, J., Wang, S.X., Zhu, J., Zhou, W., Tse, H.W., Mondragon-Gonzalez, R., Roma, G., and Glass, D.J. (2019). Age-related gene expression signature in rats demonstrate early, late, and linear transcriptional changes from multiple tissues. Cell Rep. *28*, 3263–3273.e3.

Song, M., Franco, A., Fleischer, J.A., Zhang, L., and Dorn, G.W. (2017). Abrogating mitochondrial dynamics in mouse hearts accelerates mitochondrial senescence. Cell Metab. *26*, 872–883.e5.

Sousa-Victor, P., García-Prat, L., and Muñoz-Cánoves, P. (2022). Control of satellite cell function in muscle regeneration and its disruption in ageing. Nat. Rev. Mol. Cell Biol. *23*, 204–226.

Sousa-Victor, P., Gutarra, S., García-Prat, L., Rodriguez-Ubreva, J., Ortet, L., Ruiz-Bonilla, V., Jardí, M., Ballestar, E., González, S., Serrano, A.L., et al. (2014). Geriatric muscle stem cells switch reversible quiescence into senescence. Nature *506*, 316–321.

Sousa-Victor, P., Neves, J., and Muñoz-Cánoves, P. (2020). Muscle stem cell aging: identifying ways to induce tissue rejuvenation. Mech. Ageing Dev. *188*, 111246.

Stegeman, R., and Weake, V.M. (2017). Transcriptional signatures of aging. J. Mol. Biol. *429*, 2427–2437.

Subramanian, A., Tamayo, P., Mootha, V.K., Mukherjee, S., Ebert, B.L., Gillette, M.A., Paulovich, A., Pomeroy, S.L., Golub, T.R., Lander, E.S., and Mesirov, J.P. (2005). Gene set enrichment analysis: a knowledge-based approach for interpreting genome-wide expression profiles. Proc. Natl. Acad. Sci. USA *102*, 15545–15550.

Suelves, M., Vidal, B., Serrano, A.L., Tjwa, M., Roma, J., López-Alemany, R., Luttun, A., de Lagrán, M.M., Díaz-Ramos, A., Jardí, M., et al. (2007). uPA deficiency exacerbates muscular dystrophy in MDX mice. J. Cell Biol. *178*, 1039–1051.

Tang, A.H., and Rando, T.A. (2014). Induction of autophagy supports the bioenergetic demands of quiescent muscle stem cell activation. EMBO J. *33*, 2782–2797.

Toyama, E.Q., Herzig, S., Courchet, J., Lewis, T.L., Losón, O.C., Hellberg, K., Young, N.P., Chen, H., Polleux, F., Chan, D.C., and Shaw, R.J. (2016). Metabolism. AMP-activated protein kinase mediates mitochondrial fission in response to energy stress. Science *351*, 275–281.

Twig, G., Elorza, A., Molina, A.J.A., Mohamed, H., Wikstrom, J.D., Walzer, G., Stiles, L., Haigh, S.E., Katz, S., Las, G., et al. (2008). Fission and selective fusion govern mitochondrial segregation and elimination by autophagy. EMBO J. *27*, 433–446.

Vincent, A.E., Ng, Y.S., White, K., Davey, T., Mannella, C., Falkous, G., Feeney, C., Schaefer, A.M., McFarland, R., Gorman, G.S., et al. (2016). The spectrum of mitochondrial ultrastructural defects in mitochondrial myopathy. Sci. Rep. *6*, 30610.

White, J.P., Billin, A.N., Campbell, M.E., Russell, A.J., Huffman, K.M., and Kraus, W.E. (2018). The AMPK/p27Kip1 axis regulates autophagy/apoptosis decisions in aged skeletal muscle stem cells. Stem Cell Rep. *11*, 425–439.

Youle, R.J., and van der Bliek, A.M. (2012). Mitochondrial fission, fusion, and stress. Science *337*, 1062–1065.

Zhang, C.-S., and Lin, S.-C. (2016). AMPK promotes autophagy by facilitating mitochondrial fission. Cell Metab. *23*, 399–401.

Zhang, H., Ryu, D., Wu, Y., Gariani, K., Wang, X., Luan, P., D'Amico, D., Ropelle, E.R., Lutolf, M.P., Aebersold, R., et al. (2016). NAD^+ repletion improves mitochondrial and stem cell function and enhances life span in mice. Science *352*, 1436–1443.

CellPress
OPEN ACCESS

STAR★METHODS

KEY RESOURCES TABLE

REAGENT or RESOURCE	SOURCE	IDENTIFIER
Antibodies		
Rabbit polyclonal anti- Citrate synthetase	abcam	Cat# ab 96600; RRID:AB_10678258
Mouse monoclonal anti- TOM20	abcam	Cat# ab56783;RRID: AB_945896
Mouse monoclonal anti- eMHC	DHSB	Cat# F1.652; RRID:AB_528358
Chicken anti- GFP	AVES Labs	Cat# GFP-1020; RRID:AB_10000240
Rabbit polyclonal anti- KI67	abcam	Cat# ab15580; RRID:AB_443209
Rabbit polyclonal anti- Laminin	Novus Biological	Cat# NB300-144AF647; RRID:AB_2891039
Rabbit polyclonal anti- MYOD	Santa Cruz	Cat# sc-760; RRID:AB_2148870
Rabbit polyclonal anti- Myogenin	Santa Cruz	Cat# sc-576;RRID: AB_2148908
Mouse monoclonal anti- PAX7	Santa Cruz	Cat# sc-81648; RRID:AB_2159836
Rabbit monoclonal anti- DRP1	Cell Signaling Technology	Cat# 8570;RRID: AB_10950498
Rabbit polyclonal anti- phospho-DRP1 (Ser616)	Cell Signaling Technology	Cat# 3455; RRID: AB_2085352
Mouse monoclonal anti- CD56 (NCAM)	Monosan	Cat# MON 9006; RRID:AB_419798
Mouse monoclonal anti- dsDNA	abcam	Cat# ab27156;RRID: AB_470907
Mouse monoclonal anti- LC3	Nanotools	Cat# 0231-100; RRID:AB_2722733
Rabbit polyclonal anti- p62/SQSTM1	Merck	Cat# P0067; RRID:AB_1841064
Rabbit polyclonal anti- Parkin	abcam	Cat# ab15494;RRID: AB_301903
Rat monoclonal anti- LAMP1	Santa Cruz	Cat# sc-19992; RRID:AB_2134495
Rabbit anti- γ-H2AX	Cell Signaling Technology	Cat# 2577; RRID:AB_2118010
Rabbit polyclonal anti- Cleaved Caspase-3 (Asp175)	Cell Signaling Technology	Cat# 9661; RRID:AB_2341188
Rat monoclonal anti- BrdU	abcam	Cat# ab 6326;RRID: AB_305426
Alexa Fluor 488 goat anti mouse	Invitrogen	Cat# A11017; RRID:AB_2534084
Alexa Fluor 488 goat anti mouse	Invitrogen	Cat# A21121 RRID:AB_2535764
Alexa Fluor 488 goat anti rabbit	Invitrogen	Cat# A11008; RRID:AB_143165
Alexa Fluor 568 goat anti mouse	Invitrogen	Cat# A21124; RRID:AB_2535766
Alexa Fluor 568 goat anti rabbit	Invitrogen	Cat# A11036; RRID:AB_10563566

(*Continued on next page*)

Continued

REAGENT or RESOURCE	SOURCE	IDENTIFIER
Alexa Fluor 568 goat anti rat	Invitrogen	Cat# A11077; RRID:AB_2534121
Alexa Fluor 647 goat anti mouse	Invitrogen	Cat# A21240;RRID: AB_2535809
Alexa Fluor 647 goat anti rabbit	Invitrogen	Cat# A21245;RRID: AB_2535813
Alexa Fluor 647 goat anti rat	Invitrogen	Cat# A21247;RRID: AB_141778
Alexa Fluor 568 goat anti chicken	Invitrogen	Cat# A11041;RRID: AB_2534098
FITC goat anti chicken	Aves Lab	Cat# F-1005; RRID:AB_2313516
PE-conjugated anti- α7-integrin	Ablab	Cat# 53-0010-05 RRID: AB_2920884
Alexa Fluor 647-conjugated anti-CD34	BD Pharmigen	Cat# 560230; RRID:AB_1645200
PE-Cy7-conjugated anti- Sca-1	Biolegend	Cat# 108114; RRID:AB_493596
PE-Cy7-conjugated anti- CD45	Biolegend	Cat# 103114; RRID:AB_312979
PE-Cy7-conjugated anti- CD31	Biolegend	Cat# 102418; RRID:AB_830757
Lentiviral constructs		
pLV[Exp]- pLV[Exp]-hPGK>{ST-DRP1(WT)}	Vector Builder, CNIC Viral Vectors Unit	N/A
pLV[Exp]-hPGK>mCherry	Vector Builder, CNIC Viral Vectors Unit	N/A
Biological samples		
Muscle biopsies from human adult subjects	Tissue Banks for Research from Vall d'Hebron and Sant J. Deu Hospitals and especially via the EU/FP7 Myoage Consortium	https://doi.org/10.1038/nature13013
Human satellite cell-derived primary myoblasts	EU/FP7 Myoage Consortium	N/A
Chemicals, dyes, and recombinant proteins		
poly-L-lysine	Sigma-Aldrich	Cat# P8920
EdU	Invitrogen	Cat# A10044
BrdU	Sigma-Aldrich	Cat# B9285
Sodium dichloroacetate (DCA)	Sigma-Aldrich	Cat# 347795
pyronin Y	abcam	Cat# ab146350
Verapamil hydrochloride	Sigma-Aldrich	Cat# V4629
Vybrant Dil Cell Labelling solution	Invitrogen	Cat# V22889
MitoTracker Red CMXRos	Invitrogen	Cat# M7512
MitoTracker Deep Red	Invitrogen	Cat# M22426
TMRM	Sigma-Aldrich	Cat# T5428
CellROX Deep Red	Invitrogen	Cat# C10422
CellTak	Corning	Cat# 354240
Lipofectamine 3000	Invitrogen	Cat# L3000001
SYTOX Green Nucleic Acid Stain	Invitrogen	Cat# S7020
Fluoromount G	Southern Biotech	Cat# 0100-01
Bovine Serum Albumin (BSA) (IgG-Free, Protease-Free)	Jackson Immono Research	Cat# 001-000-162
PowerTrack SYBR Green Master Mix	Roche	Cat# A46012
SuperScriptTM III Reverse Transcriptase	Invitrogen	Cat#18080-044

(*Continued on next page*)

Continued

REAGENT or RESOURCE	SOURCE	IDENTIFIER
Liberase	Roche	Cat# 5401020001
Dispase	Sigma-Aldrich	Cat# D4693-1G
Lysis Buffer	eBioscience	Cat# 00-4333-57
Hematoxylin	Sigma-Aldrich	Cat# HHS80
Eosin	Sigma-Aldrich	Cat# 45235
Tamoxifen	Sigma-Aldrich	Cat# T5648
Cardiotoxin	Latoxan	Cat# L8102
Hams F10 medium	Biowest	Cat# L0140-500
Myotonic basal medium	Cook MyoSite	Cat# MB-2222
MyoTonic growth supplement	Cook MyoSite	Cat# MS-3333
b-FGF	Peprotech	Cat# 100-18B-250UG
Critical commercial assays		
DAB Substrate Kit Peroxidase (HRP), with Nickel, (3,3'-diaminobenzidine)	Vector Laboratories	Cat# SK-4100
Click-iT EdU Imaging Kit	Invitrogen	Cat# C10337
ATP Bioluminescence Assay Kit CLS II	Roche	Cat# 11699695001
CyQUANT NF Cell Proliferation Assay Kit	Invitrogen	Cat# C35006
PicoPure RNA Isolation Kit	ARN ARCTURUS	Cat# KIT0204
RNeasy Micro Kit	QIAGEN	Cat# 74004
First-Strand cDNA Synthesis kit	Roche	Cat# 11483188001
Deposited data		
Raw and analyzed data	This paper	GEO: GSE183643
Experimental models: Organisms/strains		
Mouse: C57BL/6J	The Jackson Laboratory	RRID:IMSR_JAX:000664
Pax7^{CreEr};ROSA^{YFP}	Nishijo et al., 2009	provided by Dr. C. Keller
Drp1$^{foxl/flox}$	Ishihara et al., 2009	provided by Dr. L. Scorrano
Oligonucleotides		
ON-TARGETplus siRNA Mfn1-SMARTpool	Dharmacon	Cat# L-065399-00-0005
ON-TARGETplus siRNA Pdk1-SMARTpool	Dharmacon	Cat# L-054066-00-0005
ON-TARGETplus siRNA Pdk2-SMARTpool	Dharmacon	Cat# L-051566-00-0005
ON-TARGETplus siRNA Pdk3-SMARTpool	Dharmacon	Cat# L-052920-00-0005
ON-TARGETplus siRNA Pdk4-SMARTpool	Dharmacon	Cat# L-043425-00-0005
ON-TARGETplus Non- targeting Pool	Dharmacon	Cat# D-001810-10-05
Software and algorithms		
Fiji	Open Source	RRID:SCR_002285; http://fiji.sc
Imaris	Oxford Instruments	https://imaris.oxinst.com/
Graphpad Prism 8.0	GraphPad Software, Inc.	RRID:SCR_002798; https://www.graphpad.com
FlowJo	Tree Star Inc.	https://www.flowjo.com/solutions/flowjo/downloads
FastQC 0.11.8	Babraham Bioinformatics	https://www.bioinformatics.babraham.ac.uk/projects/fastqc/
Ensembl GRCm38, release 81	Cunningham et al., 2015	http://ftp.ensembl.org/pub/release-81/
R	R Core Team	https://www.r-project.org/
DESeq2 1.28.1	Love et al., 2014	http://bioconductor.org/packages/release/bioc/html/DESeq2.html
edgeR 3.30.0	Robinson et al., 2010	http://bioconductor.org/packages/release/bioc/html/edgeR.html
g:Profiler web server	Raudvere et al., 2019	https://biit.cs.ut.ee/gprofiler/gost

(*Continued on next page*)

Continued

REAGENT or RESOURCE	SOURCE	IDENTIFIER
GSEA 4.0.1	Subramanian et al., 2005	http://www.gsea-msigdb.org/gsea/index.jsp
Reactome	Jassal et al., 2020	https://reactome.org/
MSigDB 5.1	Liberzon et al., 2011	https://www.gsea-msigdb.org/gsea/msigdb
Cytoscape 3.8.0	Shannon et al., 2003	https://cytoscape.org/
EnrichmentMap 3.2.1	Merico et al., 2010	http://www.baderlab.org/Software/EnrichmentMap
AutoAnnotate 1.3.2	Kucera et al., 2016	http://apps.cytoscape.org/apps/autoannotate
Gene Ontology	The Gene Ontology Consortium	http://geneontology.org/
STRING	STRING Consortium	https://string-db.org/
Other		
15-well chamber slide (μ-Slide Angiogenesis)	Ibidi	Cat# 81506
Seahorse XFe96 FluxPak	Agilent	Cat# 102416-100

RESOURCE AVAILABILITY

Lead contact

Further information and requests for resources and reagents should be directed to and will be fulfilled by the Lead Contact, Pura Munoz-Canoves (pura.munoz@upf.edu).

Materials availability

This study did not generate new unique reagents.

Data and code availability

- Single-cell RNA-seq data have been deposited at GEO and are publicly available as of the date of publication. Accession numbers are listed in the key resources table. Data reported in this paper will be shared by the lead contact upon request.
- This paper does not report original code.
- Any additional information required to reanalyze the data reported in this paper is available from the lead contact upon request.

EXPERIMENTAL MODEL AND SUBJECT DETAILS

Mice

Male mice C57BL/6J (wild type, WT), C57BL/6N (WT), and the offspring of crossing *Drp1*$^{fl/fl}$ (Ishihara et al., 2009) (generously provided by L. Scorrano, University of Padova) with *Pax7*$^{CRE\text{-}ER}$;*ROSA26*^{YFP} line (Nishijo et al., 2009) (kindly provided by Dr. C. Keller) (*Drp1*$^{\Delta Pax7ER}$;*ROSA26*^{YFP}) were used at indicated ages. In *Drp1*$^{\Delta Pax7ER}$;*ROSA26*^{YFP} and, the deletion of the *Drp1* gene is inducible in satellite cells. The *Pax7*^{CreER} mouse line (Nishijo et al., 2009) was kindly provided by Dr. C. Keller). *Pax7*$^{CRE\text{-}ER}$;*ROSA26*^{YFP} or the CRE negative littermates were used as controls. In aging studies, female mice of different ages from the same WT lines were used. No statistical methods were used to predetermine sample size. All animal experiments and procedures were approved by the CNIC Institutional and Regional animal research committees of the Madrid and Catalan Governments using sex-, age- and weight-matched littermate mice.

Human samples

Muscle biopsies from human adult subjects were obtained via the Tissue Banks for Research from Vall d'Hebron and Sant Joan de Deu Hospitals (Barcelona), and especially via the EU/FP7 MyoAge Consortium. Muscle biopsies were taken from the vastus lateralis muscle under local anesthesia (2% lidocaine). A portion of the muscle tissue was directly frozen in melting isopentane and stored at −80 °C. Human satellite cell-derived primary myoblasts from 3 young/adult (25 ± 4 years old) and 4 aged (75 ± 4 years old) subjects were obtained from the EU/FP7 Myoage Consortium or purchased from Cook Myosite and cultured following the provided instructions.

Mouse satellite cell isolation by FACS

Collected muscles were minced manually and dissociated in DMEM media containing Liberase (0.1 mg/g muscle weight) (Roche, 5401020001; 5 mg/ml) and Dispase (Sigma-Aldrich, D4693-1G) 0.3% at 37 °C for 1 h using the gentleMACS Octo Dissociator (Miltenyi Biotec, 130-095-937) or 1.5 h using the conventional water bath. The muscle homogenate was then filtered and pelleted. Cells were incubated in lysis buffer (eBioscience, 00-4333-57) for 5 min on ice, resuspended in PBS with 1% goat serum (FACS buffer), and counted. PE-Cy7-conjugated anti-CD45 (Biolegend, 103114) and anti-Sca-1 (Biolegend, 108114), PE-Cy7-conjugated anti-CD31 (Biolegend, 102418) antibodies were used for lineage-negative selection and Alexa Fluor 647-conjugated anti-CD34 (BD Pharmigen, 560230) and PE-conjugated anti-α7-integrin (AbLab, 53-0010-05) were used for double-positive staining of quiescent satellite cells. Cells were sorted using a FACS Aria II (BD) sorter. Isolated satellite cells were collected in lysis buffer for RNA extraction or FACS buffer for ATP and mtDNA quantification. For cell culture, proliferation assay, and immunofluorescence (IF) staining, cells were collected in growth medium (GM) (Hams F10 (Biowest, L0140-500): DMEM 1:1 supplemented with 20% fetal bovine serum (FBS, Sigma-Aldrich F7524), 1% Penicillin/Streptomycin (P/S, Sigma-Aldrich, 15140-122) and 1% L-glutamine (Lonza, 17-605E) and bFGF (PEPROTECH, 100-18B; 0025 μg mL^{-1})).

Primary cell cultures

Mouse primary satellite cells were maintained in collagen-coated plates and growth medium (GM). For coating, collagen (3 mg/ml) was added to the cell culture plate to cover the full surface, incubated at 37 °C for 30 min, and removed and washed once with sterile PBS. For human cell studies, human primary myoblasts were maintained in Myotonic basal medium (MB-2222) supplied with MyoTonic growth supplement (MS-3333) and 1% P/S. The medium was changed every other day. The medium was changed every other day and the cell confluency was maintained below 50%. All cells were maintained at 37 °C with 21% O_2 and 5% CO_2 unless otherwise indicated.

METHOD DETAILS

Animal procedures

CRE activity was induced by intraperitoneal injection (one injection per day for 4 continuous days) with 2 mg/30 g body weight tamoxifen (TMX) (Sigma; 20 mg/ml in corn oil) and experiments were carried out at 21 days post-TMX induction. For muscle regeneration experiments, mice were anesthetized with isoflurane inhalation. Regeneration of skeletal muscle was induced by intramuscular injection of cardiotoxin (CTX, Latoxan) in the tibialis anterior (TA), gastrocnemius, and quadriceps muscle of the mice as previously described (Suelves et al., 2007). At the indicated times after injury, mice were euthanized and muscles were dissected, incubated in OCT and snap-frozen in an isopentane/liquid nitrogen double bath, and stored at -80 °C until analysis. For GFP and YFP immunostaining samples and specially indicated samples, muscle samples were prefixed 2 h in 2% PFA at 4°C, washed and embedded in 30% sucrose at 4 °C, and then frozen in an isopentane/liquid nitrogen double bath.

Genotyping of mice

For mice genotyping, the following PCR primers were used: Drp1 flox (Fw) 5′-CAGCTGCACTGGCTTCATGACTC-3; Drp1 flox (Rv) 5′-GTCAACTTGCCATAAACCAGAG-3′. ROSA: (R316)5′- GGAGCGGGAGAAA TGGATATG-3′; (R883) 5′-AAAGTCGCTCTGAGTTGT TAT-3′ (R4982) 5′-AAG ACCGCGAAGAGTTTGTC-3. CRE pblast (Fw): 5-CCCGCAGAACCTGAAGATGT-3; CRE pblast (Rv) 5′-CAGCGTTTTCGTTCTGCCAA-3′; Actin-S: 5′-TCATCAG GTAGTCAGTGAGGTCGC-3′; Actin-AS: 5′-CACCACACCTTCTACAAT GAGCTG-3′.

Satellite cell transplantation

Cell transplants were performed as described in (Sacco et al., 2010), following an adapted protocol (Sousa-Victor et al., 2014). 10,000 cells were injected with a Hamilton syringe into pre-injured muscles of immunodeficient (recipient) mice (Le et al., 2016). 4 days after cell injections, engrafted muscles were collected and processed for muscle histology.

For treatments with lentiviral particles: Recombinant lentiviruses (LV) for expressing the human DRP1 wt form (LV-DRP1) or a fluorescent reporter gene instead as control (LV-control), were custom-designed and assembled using the Vectorbuilder platform (Vectorbuilder). Briefly, the LVs consist of a third-generation lentiviral vector backbone containing the human dynamin-like 1 (*DNML1*) ORF expression cassette driven by the human phosphoglycerate kinase 1 (hPGK) promoter, and packed in a VSV-G envelope in our in-house viral vector facility. For lentiviral ex-vivo transductions, freshly FACS-isolated satellite cells were collected in GM and plated in six-well plates coated with collagen (3 mg/ml, 40-50 k cells/well) overnight as described previously ((García-Prat et al., 2020b)).

For rapamycin and Urolinthin A treatment: FACS-isolated satellite cells were collected in GM, plated on collagen-treated plates, and treated for 48 h with Rapamycin (100 ng/ml, LC Laboratories), Urolinthin A (Tocris, 100 μM) or vehicle (DMSO), to reactivate autophagy as described in (García-Prat et al., 2016). The rapamycin/vehicle or Urolithin A/vehicle treated cells were labeled with Vybrant Dil Cell Labelling solution (Invitrogen, #V22889) according to manufacturer instructions before engraftment as previously described (García-Prat et al., 2020).

For siRNA treatment: FACS-isolated satellite cells were collected in GM and transfected with siRNA for 3h on ice and transplanted, as previously described (García-Prat et al., 2020). For the transfection, Lipofectamine 3000 reagent (Invitrogen) was applied according to the manufacturer's instructions with 20 nM of ON-TARGETplus non/targeting siRNA control pool or ON-TARGETplus siRNAs targeting the following genes:

Target gene	Target sequence	Target gene	Target sequence
Mfn1	CGAAAGAGAGAGAGUUUAA	Pdk1	CAAUACAAGUGGUUUAUGU
	CAGCAAGAAAUCAUCGAAA		CCUGUUAGAUUGGCAAAUA
	AGGGAAGACCAAAUCGAUA		UCAAUUAGAAUGCUACUCA
	GGAGAAUCCUAACGGCAGA		GGUUACGGAUUGCCCAUAU
Pdk2	CGACGUAUCGGGUCAGCUA	Pdk3	UAAUGUAGCUGAUGUGGUU
	GAGGACCACCGGACUCUAA		GACAAGAUCAAGAGUAAUA
	GAUCCCAACUGCAGCGUGU		AGACUUGUCCAUUAAGAUA
	GAGAAGACGUCAUUCACUU		CGAAACAUAUAGGGAGUAU
Pdk4	AGUCAGCCUUCAAACAUUA		
	GUACGUUCCUUCACACCUU		
	CGACCAGUAUUAUCUAACA		
	GAUCUGAAUCUCUACUCUA		

In vivo DCA treatment

TA muscle of each mouse (old WT mice and young DRP1 mice) was injured with CTX. On the same day of the injury, sodium dichloroacetate (DCA, Sigma 347795) or vehicle (saline) was administered daily subcutaneously for four days, over the lesioned area (5 mg/100 μl). For samples containing YFP$^+$ cells (*Drp1*^{WT};*ROSA26*^{YFP} vs *Drp1*$^{\Delta Pax7ER}$;*ROSA26*^{YFP}), at 4-days post-injury, the muscles were collected and cut in two parts at the cross-section in the middle of the muscle. One part of the muscle was incubated in OCT and snap-frozen in an isopentane/liquid nitrogen double bath whereas the other half was cryo-preserved (fixed in 2% PFA at 4°C for 2 h, washed, and embedded in 30% sucrose at 4 °C) and then frozen in isopentane/liquid nitrogen double bath. For samples without YFP (WT young *vs* old), the TA muscle was incubated in OCT and snap-frozen in an isopentane/liquid nitrogen double bath. Samples were stored at -80 °C until analysis. All experiments requiring YFP IF were carried out using the cryo-preserved samples whereas other experiments (eMHC IHC, other IF stainings) were carried out using snap-frozen samples.

Ex vivo transfection and infection

For the siRNA transfection, Lipofectamine 3000 reagent (Invitrogen) was applied according to the manufacturer's instructions with 20 nM of ON-TARGETplus non/targeting siRNA control pool or ON-TARGETplus siRNAs. Lipofectamine and siRNA were first diluted in Opti-MEM medium separately. The siRNA prep was mixed with the lipofectamine prep at 1:1 and the mixture was incubated at RT for 15 min before being added into the cell culture medium drop by drop. The total mixture volume added is 10% of the final total medium volume. For lentiviral infection, cells were maintained in six-well plates coated with collagen. The culture medium was moved and fresh medium supplied with polybrene (1/500, provided by VectorBuilder) was added. The cells were incubated with LV-DRP1 or LV-control for 24 h and the medium was replaced. Transduced cells were maintained in fresh medium for 3 days after lentivirus removal before further experiments were carried out to ensure the expression of DRP1 protein.

Ex vivo analysis of autophagy/mitophagy flux

FACS-isolated satellite cells were seeded into wells of a 15-well chamber slide (Ibidi μ-Slide Angiogenesis 81506) coated with 0.01% poly-L-lysine (Sigma-Aldrich, P8920) at a density of 2000-3000 cells/well. Bafilomycin A (10 nM Sigma B1793) was added to the cells for 4 h at 37 °C. At 3.5h after the treatment, 100 nM MitoTracker Red CMXRos was added to the cells and incubated for another 30 min at 37 °C in dark. After that, the cells were fixed with 4% PFA, washed with PBS, and either proceed directly for immunofluorescence staining or sealed and stored at 4 °C.

Ex vivo DCA treatment

DCA was dissolved in PBS and stored as 1M stock. For treatment, a final concentration of 2 mM and 5mM DCA was used and PBS was used as vehicle.

Histology and immunohistochemistry (IHC) in muscle cryosections

TA muscles were snap-frozen or pre-fixed (4% PFA 2 h at 4 °C and washed in PBS), cryo-preserved and frozen in an isopentane/liquid nitrogen double bath, and stored at -80 °C until analysis. Hematoxylin/eosin (HE), immunochemistry, and IF staining were performed in 10 μm sections. Labeling of cryosections with embryonic myosin heavy chain was performed using the peroxidase M.O.M

kit staining (Vector Laboratories, SK-4100) according to the manufacturer's instructions. Double immunostaining was performed by sequential addition of each primary and secondary antibody using appropriate positive and negative controls. For snap-frozen samples, sections were air-dried, fixed on PFA 4%, washed on PBS, and permeabilized with ice-cold methanol before antigen retrieval. For antigen retrieval, the sections were incubated in boiling citric acid (0.01 M, pH=6) for 10 min, cooled, and washed with PBS. For pre-fixed TA muscles, 0.5% Triton-100 was used for permeabilization and no antigen retrieval was performed. The samples were then incubated with primary antibodies according to the manufacturer's instructions after blocking for 1 h at room temperature (RT) with 5% BSA and M.O.M blocking diluted in PBS (30 min). Subsequently, the slides were washed on PBS and incubated with appropriate secondary antibodies and labeling dyes. For immunofluorescence, secondary antibodies were coupled (see below) and nuclei were stained with DAPI (Invitrogen) or SYTOX Green Nucleic Acid Stain (Invitrogen, S7020). After washing, tissue sections were mounted with Fluoromount G (SouthernBiotech). Selected primary and secondary antibodies were applied (See key resources table).

Immunofluorescence (IF) in isolated satellite cells

Satellite cells isolated from FACS were seeded into wells of a 15-well chamber slide (Ibidi μ-Slide Angiogenesis, 81506) coated with 0.01% poly-L-lysine (Sigma-Aldrich, P8920) at a density of 2000-3000 cells/well. The cells were fixed with 4% PFA, washed with PBS, permeabilized with 0.5% Triton-100 and blocked with 3% BSA for 1h at RT. Selected primary and secondary antibodies were applied (See key resources table).

Mitochondrial morphology analysis

A minimum of 5,000 satellite cells were mixed with MitoTracker Red CMXRos (Invitrogen, M7512, 100 nM) and plated in 15-well angiogenesis Ibidi chambers pre-coated with 0.01% poly-L-lysine and incubated at 37°C for 45 min. After incubation, half the volume of the medium was carefully removed and replaced with the same volume of 8% electron microscope standard PFA. The cells were incubated in PFA for 10 min, washed, and stored in PBS before IF staining. Before imaging, other IF staining could be performed and the wells were mounted with Fluoromount G. Z-stack images were acquired by Leica SP8 microscope with pinhole = 0.5A, Z = 250 nm. Acquired images were processed with Huygens professional deconvolution software. Specifically, automatic estimation of background (lowest mode, area radius = 0.7 μm) and a CMLE algorithm (maximum iterations = 30; signal to noise ratio = 15; quality threshold = 0.05 with optimized iteration mode and automatic brick layout) was applied for the deconvolution. All images were batch-processed with the same algorithm. The processed images were then loaded to the Imaris 3 software for 3D reconstruction and surface analysis using the surface-creating function.

Proliferation assays

To assess satellite cell proliferation *in vivo*, muscles were injured by local CTX injection, and mice were administered with ethynyl-labeled deoxyuridine (EdU, Invitrogen, #A10044; 25.5 mg/kg; i.p.) 4 hours before the sacrifice at 3-4-DPI. Muscles were collected and processed for immunofluorescence staining in tissue slides or cell isolation by FACS. EdU-labeled cells were detected using the Click-iT EdU Imaging Kit (Invitrogen, #C10086). EdU-positive cells were quantified as the percentage of the total number of cells analyzed. Proliferation assays of human satellite cell-derived primary myoblasts from young and aged human individuals (see above) were cultured in MyoTonic basal medium (MB-2222) with Myotonic growth supplement (MB-3333), and cells were pulse-labeled with bromodeoxyuridine (BrdU, Sigma-Aldrich, #B9285-1G; 1.5 μg/ml) for 1 h. BrdU-labeled cells were detected by immunostaining (Abcam, #AB6326; 1:500). Antibody binding was visualized using Vectastain Elite ABC reagent (Vector Laboratories, #PK-6100) and 3,3'-Diaminobenzidine (DAB). BrdU-positive cells were quantified as the percentage of the total number of cells analyzed.

ATP content analysis

10,000 sorted satellite cells were pelleted and boiled in 100 mM Tris, 4 mM EDTA, pH 7.74 for 2 min. After boiling, the samples were centrifuged and the supernatant was used for analysis. ATP levels were measured using the ATP Bioluminescence Assay Kit CLS II (Roche) according to the manufacturer's instructions. Samples and ATP standard mixtures were mixed with one equal volume of luciferase and measured immediately in a luminometer (Berthold Detection Systems).

mtDNA quantification

10,000 sorted SCs were pelleted and lysed overnight (O.N.) in 150 μl Bradley lysis buffer (10 mM TRIS-HCL pH 7.5; 10 mM EDTA; 0.5% SDS; 10 mM NaCl in ddH_2O) with proteinase K (0.5 mg/ml) at 56 °C. Once cooled down to RT, samples were incubated with RNase A (100 μg/ml, Thermo Fisher #EN0531) at 37 °C for 30 min, and cooled down to RT. samples were precipitated with 300 μl ice-cold EtOH/NaCl (75 mM NaCl in 100% EtOH) mix for 30 min at RT. The samples were centrifuged at 13,000 xg for 15 min and the supernatant was discarded. The pellet was washed twice with ice-cold 70% EtOH and the liquid was discarded and evaporated at RT. The dried pellet was resuspended in 20 μL TE buffer and incubated at 56 °C for 10 min. mtDNA was quantified by RT-qPCR using primers amplifying the Cytochrome b region on mtDNA (forward primer: 5′-CATTTATTATCGCGGCCCTA-3′, reverse primer: 5′-TGTTGGGTTGTTTGATCCTG-3′), relative to the β-actin region on gDNA (forward primer: 5′-CGGCTTGCGGG TGTTAAAAG-3′, reverse primer: 5′-CGTGATCGTAGCGTCTGGTT-3′). 10 μl reaction volume for each well was loaded (1.5 μl DNA (2.5 ng/μl), 0.25 μl 10 mM forward and reverse primer, 5 μl SYBR green reagent, and 3 μl H2O). $2^*(2^{\Delta Ct})$ was presented as the read-out (ΔCt= genomic Ct-mitochondrial Ct).

Cellular metabolic analysis

Cell oxygen consumption was measured using either the Seahorse XF96 Extracellular Flux Analyzer or the Oxygraph-2k (Oroboros).

For Seahorse analysis, satellite cells were sorted into GM. The cells were then placed into an XF96-well plate pre-coated with CellTak (Corning®, 354240 following manufacturer's instructions) at a density of 80 k/well (quiescence) or 30 k/well (3-DPI). For experiments that require 48h *in vitro* treatments before Seahorse analysis (siRNA, DCA), 20k quiescent satellite cells/well or 8k proliferating myoblasts/well were seeded. After a gentle centrifuge (5 min, 50g), the medium in each well was carefully removed without drying out the well and re-supplied carefully with 200 μl GM. For quiescence studies, the cells were maintained in hypoxia (3% O_2, 5%CO_2) for 6 h before the Seahorse analysis. XF-calibrant (Agilent, 100840) and cartridge submerged in ddH_2O were maintained in CO_2-free Seahorse incubator O.N. On the day of the Seahorse assay, GM was replaced with XF medium (phenol red-free DMEM pH = 7.4 supplied with 25 mM glucose, 1 mM sodium pyruvate, and 2 mM glutamine) and incubated in a CO_2-free Seahorse incubator for at least 45 min before the assay to deplete CO_2. Selected drugs were dissolved in phenol red-free DMEM (pH = 7.4 supplied with 2 mM glutamine) at desired concentrations (final working concentration 1 μM for oligomycin, FCCP, rotenone + antimycin A). The cartridge was then submerged in a calibration medium and drugs were loaded into the loading ports of the cartridge (25 μl/port). After calibration, the calibration plate was replaced by a cell plate as indicated by the Seahorse program. At the end of the assay, a normalization step was applied using CyQUANT NF Cell Proliferation Assay Kit (Invitrogen C35006). Briefly, the assay medium was replaced with CyQUANT normalization medium applied (50 μl/well) and the plate was incubated at 37 °C for 30 min and protected from light until the end of the procedure. The emission was analyzed in a fluorometer (filters: excitation 485 nm, emission 538 nm) as an indicator for protein content.

For oxygraph analysis, proliferating primary progenitors were trypsinized, counted, and resuspended in mitochondrial respiration medium (Mir05 Respiration Buffer, Oroboros Instruments). 300 k cells were loaded into the 0.5 ml chamber of the Oroboros instrument. For analyzing the respiration of each mitochondrial complex, the cells were permeabilized with 3 μg digitonin and the following substrates and inhibitors were sequentially injected: 5mM pyruvate, 10mM malate, 2.5 mM ADP (complex I respiration), 10 mM succinate (complex I +II respiration), 0.5 μM rotenone (complex II respiration), 2.5 μM antimycin A (non-mitochondrial respiration), 2 mM TMPD, 0.5 mM ascorbate (complex IV respiration) and 100 mM sodium azide (correction of complex IV respiration). The oxygen consumption was expressed as pmol O_2 consumed per second per ml per million cells and the data was normalized to the level of WT cells in each experiment.

Flow cytometry assays

For mitochondrial membrane potential assay, satellite cells were sorted into GM and incubated with TMRM (50 nM) at 37 °C for 30 min, CCCP 5 μM was applied in parallel as a control. TMRM signal was obtained using BD LSRFortessa flow cytometer. For the mitochondrial content assay, satellite cells were resuspended in staining buffer (FACS buffer supplied with 50 μM Verapamil hydrochloride (Sigma, V4629)) and incubated with MitoTracker Red CMXRos (Invitrogen, M7512, 100 nM) or MitoTracker Deep Red (Invitrogen, M22426, 100 nM) at 37 °C for 30 min. For the pyronin Y assay, cells were resuspended in staining buffer and incubated in 1 μg/ml pyronin Y (abcam, ab146350) at 37 °C for 45 min and vortexed every 15 min. At the end of the staining, the cells were washed with ice-cold staining buffer and resuspended in an appropriate volume of ice-cold staining buffer. Median fluorescence intensity (M.F.I.) was calculated using FlowJo software.

CellRox assay

Freshly-sorted satellite cells were mixed with staining medium (5 μM CellROX Deep Red, 100 nM MitoTracker Red CMXRos) and loaded onto a 15-well chamber slide (Ibidi μ-Slide Angiogenesis 81506) coated with 0.01% poly-L-lysine at a density of 2,000-3,000 cells/well. The chamber was then incubated at 37 °C for 30 min after a gentle centrifuge step (5 min, 50 xg). The staining medium was carefully removed and the cells were fixed with 3.7% formaldehyde for 15 min, washed with PBS, and imaged within 24 hours. Total CellRox$^+$ puncta and mitochondria-located CellRox puncta were quantified.

RT-qPCR

Total RNA was isolated from FACS-isolated satellite cells using PicoPure RNA Isolation Kit (ARN ARCTURUS, KIT0204) and analyzed by RT-qPCR and next-generation sequencing (NGS) as described above. For experiments using proliferating myoblasts, RNA extraction was performed using RNeasy Micro Kit (QIAGEN, 74004) according to the manufacturer's instructions. For qPCR experiments, DNase digestion was performed following the manufacturer's instructions (QIAGEN). Complementary DNA (cDNA) was synthesized from 50 ng of total RNA using the First-Strand cDNA Synthesis kit (Roche). Real-time PCR reactions were performed on an AB7900-FAST-384 System using Light Cycler 480 SYBR Green I Master reaction mix (Roche Diagnostic Corporation) and specific primers. Thermocycling conditions were as follows: an initial step of 10 min at 95 °C, then 50 cycles of 15 s denaturation at 94 °C, 10 s annealing at 60 °C, and 15 s extension at 72 °C. Reactions were run in triplicate and analyzed using SDS v2.3 Software. The detected threshold cycle (Ct) values were compared between samples. Transcripts of Tbp were used as the housekeeping gene.

List of Taqman primers used in this study:

Gene	Forward primer sequence	Reverse primer sequence
Drp1	5′-GCGCTGATCCCGCGTCAT-3′	5′-CCGCACCCACTGTGTTGA-3′
Mfn1	5′-TTACTCAGTGGAACACCGCC-3′	5′-TTGGAGAGCCGCTCATTCACCT-3′
Pdk1	5′-TTACTCAGTGGAACACCGCC-3′	5′- GTTTATCCCCCGATTCAGGT -3′
Pdk2	5′-GAAGAATGCGTCCCTGGCAG-3′	5′-GGTTCCGGATGGTGACCAGG-3′
Pdk3	5′-TCCTGGACTTCGGAAGGGATA-3′	5′- GAAGGGCGGTTCAACAAGTTA-3′
Pdk4	5′-CCCGCTGTCCATGAAGCAGC-3′	5′-CCAATGTGGCTTGGGTTTCC-3′
Tbp	5′-ATCCCAAGCGATTTGCTG-3′	5′-CCTGTGCACACCATTTTTCC-3′

Western blotting

Preparation of mouse and human satellite cell lysates and Western blotting were performed as described previously (Perdiguero et al., 2011). Antibodies used were: anti-pDRP1^{S616} antibody produced in rabbits (CST #3455) and Tubulin (Sigma T-6199).

Transmission electron microscopy

Cultured proliferating myoblasts derived from YFP^{+} *Drp1*^{WT} or *Drp1*$^{\Delta Pax7ER}$ satellite cells were prefixed with a 1:1 volume of culture medium and fixation buffer (a mixture of 2.5 % glutaraldehyde–2 % paraformaldehyde in 0.1 M sodium cacodylate buffer pH 7.2 for 24 h) for 10 min at RT and the cells were harvested and pelleted. The pellet was then incubated at 4 °C in pure fixation buffer overnight and post-fixed in 1 % osmium tetroxide for 1 h at 4 °C in the same buffer. The pellets were dehydrated in an ascending series of ethanol (50%, 70%, 90%, and 100%) in steps of 20 min each and transferred to propylene oxide (2 x 20 min). Afterward, the specimens were sequentially infiltrated in EMbed 812 resin (EMS, USA). We used the sequence propylene oxide–resin 2:1, 1:1, and 1:2 throughout 24 h (8 h each). Then, samples were transferred to pure resin for 24 h. Resin blocks were then formed in silicone molds with fresh resin for 48 h at 65 °C. We placed the samples into the molds to obtain longitudinal sections of the tissues. After trimming, blocks were sectioned in an Ultracut Reicher ultramicrotome. Thin sections (50-70 nm thick) were mounted on nickel grids. After staining in aqueous 4% uranyl acetate and lead citrate, the sections were examined and photographed in a Jeol JEM 1400 electron microscope at the Servicio Centralizado de Apoyo a la Investigación (SCAI; University of Córdoba; Spain).

RNA-seq sample and library preparation

RNA-seq of FACS sorted quiescent, 1-DPI, 3-DPI SCs from *Drp1*$^{\Delta Pax7ER}$ and *Drp1*^{WT} as well as from young and aged mice was performed as follows: 500 pg of total RNA were used for preparing RNA-seq libraries using the NEBNext Single Cell/Low Input RNA Library Prep Kit for Illumina (New England Biolabs) according to the manufacturer's instructions. Libraries were sequenced on a HiSeq 2500 (Illumina) to generate 60 base single-end reads. FastQ files for each sample were obtained using bcl2fastq 2.20 software (Illumina). NGS experiments were performed in the Genomics Unit of the CNIC.

Bulk RNA-seq Data Pre-processing

Reads were pre-processed using a pipeline that used FastQC (Babraham Institute, https://www.bioinformatics.babraham.ac.uk/projects/fastqc/), to assess read quality, and Cutadapt (Martin, 2011) to trim sequencing reads, eliminating Illumina adaptor remains, and to discard reads that were shorter than 30 bp. The resulting reads were mapped against reference transcriptome GRCm38 and gene expression levels were calculated with RSEM (Li and Dewey, 2011), whose output includes raw count estimates, as well as Transcript per million (TPM) values. Raw count estimates (expected expression counts) were used to calculate trimmed mean of M-values (TMM)-normalized counts per million (CPM) values using Bioconductor package edgeR (Robinson et al., 2010).

Differential gene expression and pathway enrichment analysis

For the differential analysis of gene expression, we considered only the genes with more than 4 CPM in all but one sample in at least one experimental group. Differentially expressed genes were found using Bioconductor package limma (Ritchie et al., 2015) with voom transformation, robust regression method for linear modeling, and empirical Bayes statistics. Genes with adjusted p-value < 0.05 were considered for further analysis. Pathway enrichment was performed using the following protocol (Reimand et al., 2019). DE genes (adjusted p-value < 0.05) were analysed on g:Profiler platform (https://biit.cs.ut.ee/gprofiler/gost). Total annotated genes from the full reference genome were used as the reference set and a Benjamini-Hochberg FDR method was applied.

Gene Set Enrichment Analysis (GSEA) and Cytoscape

Transcript per million (TPM) matrix of genes expressed with at least 1 TPM in at least three samples served as an input for GSEA software (Subramanian et al., 2005). We used the signal-to-noise metric to rank the genes, 1000 permutations with the gene set permutation type, and weighted enrichment statistics. Gene set sizes were chosen as 15-500 for MSigDB 7.1 Gene Ontology and Canonical Pathways (Liberzon et al., 2011). Gene sets passing FDR < 0.075 thresholds were subjected to further analysis. Network representation and clustering of GSEA results were performed using EnrichmentMap (version 3.2.1) and AutoAnnotate (version 1.3.2) for Cytoscape (3.8.0) with the Jaccard coefficient set to 0.375.

Comparative enrichment analysis using previously published aging dataset

We used the minimum hypergeometric test implemented in R package mHG for the comparative enrichment analysis of senescent cells and previously published aging datasets: mouse, rat, African turquoise killifish, and human (Benayoun et al., 2019; Shavlakadze et al., 2019; Stegeman and Weake, 2017). Data processing and analysis were performed as described before (Benayoun et al., 2019) with the following modifications: (1) differential expression analysis of satellite cells was performed using Bioconductor package limma, (2) to assess the differential expression for rat, killifish, and human datasets the Bioconductor DESeq2 (Love et al., 2014) 1.28.1 package version was used (instead of DESeq2 version 1.6.3), (3) both genders were analyzed for human dataset, (4) conversion to human orthologs was performed before the enrichment with MSigDB 5.1 hallmarks for all datasets except the Benayoun's mouse tissues, for which we took previously published enrichment results.

QUANTIFICATION AND STATISTICAL ANALYSIS

Digital image acquisition and analysis

Digital images were acquired using: (1) confocal images of isolated satellite cells and muscle sections were taken using an inverted Leica gated STED-3X- WLL SP8 confocal system with an HC PL Apo CS2 100×/1.4 NA or 63x/1.4 NA oil objective. (2) Low magnification IF images of muscle tissues were obtained using an inverted Nikon ECLIPSE Ti-TimeLapse microscope with a Plan Apo λ 20x/0,75 NA objective. The different fluorophores (3 to 4) were excited using the 405, 488, 568, and 633 nm excitation lines. The acquisition was performed using the LAS X 3.5.6. 21594 software. (3) Muscle tissue histology sections were digitalized using the NanoZoomer-2.0RS from Hamamatsu and processed with the NDP.view2 software.

Image analysis

- To assess myofiber size, individual fibers were manually outlined and their cross-sectional area (CSA) was determined using Fiji software. All eMHC$^+$ fibers from each muscle cross-section were quantified. In each experiment, data were obtained from 3-6 mice per group. Analysis was performed blinded.
- To quantify the number of cells per area from tissue sections, cells were quantified manually and normalized to the analyzed area. In the case of post-injury tissues, the regenerative area was determined by the presence of centrally-nucleated fibers and immune infiltration. In each experiment, data were obtained from 3-5 fields (containing 100-200 injured fibers in regeneration; or 300-800 fibers in basal condition) per animal and 3-4 mice per group. In the case of transplanted tissues, the entire engrafted TA muscle was sectioned, stained, and imaged. The engrafted area was determined by the concentrated distribution of YFP$^+$ or DiI$^+$ cells. In each experiment, data were obtained from 3-4 mice per group. Secondary antibody-stained samples were used as the negative control. Analysis was performed blinded.
- To quantify the expression of PAX7, MYOD, and KI67 in cytospins, all DAPI$^+$ cells from 5 random fields of the well were analyzed. In each experiment, 50-150 cells per animal and 3 mice per group were analyzed. Analysis was performed blinded.
- For DRP1, CellRox, LC3, and P62 puncta quantification and colocalization with the mitochondria, cells were imaged in a z-stack and the quantification was carried out manually using Fiji. For each experiment, the same automatic or manual threshold was applied across groups and 50-100 cells per group were analyzed from at least 3 mice. Analysis was performed blinded.
- For mitochondrial morphology analysis, cell 3D images were processed in Huygens deconvolution software followed by surface analysis in Imaris 3 software (See method details). For each experiment, the same threshold was applied across groups and 50-100 cells per group were analyzed from at least 3 mice. Analysis was performed blinded.
- For quantification of mitochondrial nucleoid size, cells were imaged in a z-stack and the length of each mitochondrial nucleoid was measured manually using Fiji. For each experiment, 50-100 cells per group were analyzed from at least 3 mice. Analysis was performed blinded.
- The fluorescence intensity of selected proteins for each cell was quantified as integrated intensity (IntDen) using Fiji software. 3D images were obtained from each cell, followed by cell boundary determination, background subtraction, and Gaussian blur. And z-projection. The IntDen value was calculated from MAX projection images. Same image processing was applied to all cells across groups. In each experiment, 50-150 cells per animal and 3 mice per group were analyzed. Analysis was performed blinded.
- Gaussian blur (1.0) was applied to representative confocal images using Fiji.

Statistical analysis

The sample size of each experimental group is described in the corresponding figure caption, and all of the experiments were conducted with at least three biological replicates unless otherwise indicated. GraphPad Prism software was used for all statistical analyses except for sequencing-data analysis. Quantitative data displayed as histograms are expressed as mean ± standard deviation (represented as error bars). Results from each group were averaged and used to calculate descriptive statistics. Statistical significance was set at a P-value <0.05.